

Scales of Variability in the Equatorial Pacific Inferred from the Tropical Atmosphere–Ocean Buoy Array*

WILLIAM S. KESSLER

Pacific Marine Environmental Laboratory/NOAA, Seattle, Washington

M. C. SPILLANE

JISAO, University of Washington, Seattle, Washington

MICHAEL J. MCPHADEN AND D. E. HARRISON

Pacific Marine Environmental Laboratory/NOAA, Seattle, Washington

(Manuscript received 19 June 1995, in final form 1 February 1996)

ABSTRACT

The highly temporally resolved time series from the Tropical Atmosphere–Ocean moored buoy array are used to evaluate the scales of thermal variability in the upper equatorial Pacific. The TAO array consists of nearly 70 deep-ocean moorings arranged nominally 15° longitude and 2° – 3° latitude apart across the equatorial Pacific. The bulk of the data from the array consists of daily averages telemetered in real time, with some records up to 15 years long. However, at several sites more finely resolved data exist, in some cases with resolution of 1 minute. These data form the basis for spectral decomposition spanning virtually all scales of variability from the Brunt–Väisälä frequency to the El Niño–Southern Oscillation timescale. The spectra are used to define the signal to noise ratio as a function of sample rate and frequency, and to investigate the effects of aliasing that results from sparser sampling, such as ship-based observational techniques. The results show that the signal to noise ratio is larger in the east, mostly because the low-frequency signals are larger there. The noise level for SST varies by as much as a factor of 10 among the locations studied, while noise in thermocline depth is relatively more homogeneous over the region. In general, noise due to aliased high-frequency variability increases by roughly a factor of 10 as the sample rate decreases from daily to 100-day sampling. The highly resolved spectra suggest a somewhat more optimistic estimate of overall signal-to-noise ratios for typical ship of opportunity (VOS) XBT sampling (generally about 2) than had been found in previous studies using sparser data. Time scales were estimated for various filtered versions of the time series by integration of the autocorrelation functions. For high-passed data (periods longer than about 150 days removed), the timescale is about 5 days for both surface and subsurface temperatures everywhere in the region. Conversely, for low-passed data (the annual cycle and periods shorter than 150 days removed), the timescale is roughly 100 days. Horizontal space scales were estimated from cross-correlations among the buoys. Zonal scales of low-frequency SST variations along the equator were half the width of the Pacific, larger than those of thermocline depth (about 30° – 40° longitude). In the east, meridional scales of low-frequency SST were large (greater than about 15° latitude), associated with the coherent waxing and waning of the equatorial cold tongue, whereas in the west these scales were shorter. Thermocline depth variations had meridional scales associated with the equatorial waves, particularly in the east. Spatial scale estimates reported here are generally consistent with those found from the VOS datasets when the ENSO signals in the records of each dataset are taken into account. However, if signals with periods of 1 to 2 months are to be properly sampled, then sampling scales of 1° – 2° latitude by 8° – 10° longitude, with a 5-day timescale, are needed.

1. Introduction

The purpose of this work is to use the highly temporally resolved time series from the Tropical Atmosphere–Ocean (TAO) array of moored buoys (Hayes

et al. 1991a; McPhaden 1993) to evaluate the scales of variability in the upper-ocean thermal field of the tropical Pacific. The moorings sample ocean temperatures in the upper 500 m at a rate close to or faster than the Brunt–Väisälä frequency, with some time series extending over a decade or longer. These measurements resolve virtually all the variability of interest for climate studies and can be used to precisely define how sparser sampling would affect the interpretation of observations.

The TAO array is one component of the Tropical Pacific Thermal Monitoring System (TPTMS), which was established at the outset of the TOGA (Tropical Ocean–Global Atmosphere) program in 1985 and has

* PMEL Contribution Number 1653 and JISAO Contribution Number 330.

Corresponding author address: William S. Kessler, NOAA/Pacific Marine Environmental Laboratory, 7600 Sand Point Way NE, Seattle, WA 98115.
E-mail: kessler@pmel.noaa.gov

been modified and expanded in the ensuing years. Elements of this system include both surface and subsurface temperature measurements. Surface temperatures are provided largely through an expanded surface drifter program (Niiler et al. 1996, manuscript submitted to *J. Phys. Oceanogr.*), TAO buoy measurements near the equator, and satellite analyses (Reynolds and Smith 1994). Subsurface temperatures derive mainly from the TAO array and the volunteer observing ship expendable bathythermograph (VOS XBT) program (Meyers and Donguy 1980; Smith and Meyers 1995). The VOS program samples three or four meridional ship tracks roughly once per month, with an XBT dropped approximately every degree of latitude, and it spans a wider zonal and meridional range than the TAO array.

The success of any observing system must be determined by its ability to resolve the variability of interest. The TPTMS supports El Niño–Southern Oscillation forecasting by providing data for ocean climate model validation (e.g., Hayes et al. 1989) and data for initializing coupled ocean–atmosphere climate prediction schemes (Ji et al. 1995), as well as several distinct research efforts; these activities point to several clear scales of interest. The first perspective comes from the linear theory of equatorial waves, which indicates that the zonal scale of forced motions is related to the zonal scale of the wind forcing and that, away from the forcing region, their meridional scale is determined both by the forcing and the meridional scales of free waves. The fastest response arises from low-vertical-mode Kelvin waves, with timescales comparable to the wind forcing; data on these scales are needed for validation and improvement of tropical ocean general circulation models. The next longer scale of interest is that of monthly-to-seasonal mean variations, which must be sampled accurately in order to describe the evolution of ENSO events and the seasonal march. Reliable observations on this timescale also are required for evaluation of existing models of the coupled ocean–atmosphere system; most ENSO forecasting studies are carried out on this timescale. Finally, interannual and lower-frequency variability needs to be resolved in order to determine the low-frequency changes in ENSO statistics, and the connections between ENSO and decadal-scale global climate variability.

Previous studies have estimated the observed space and time scales of the thermal field in the tropical Pacific using a variety of statistical techniques. Early observational work based on island sea levels and VOS XBT data suggested that zonal scales were quite long but that thermocline variability was usually decorrelated over a few hundred kilometers in the meridional direction (e.g., Wyrtki 1978; Meyers 1979). Barnett and Patzert (1980) analyzed 3 months of weekly airborne XBT profiles made specifically to estimate scales of variability for the purpose of planning the Hawaii-to-Tahiti Shuttle Experiment (Wyrtki et al. 1981). Kes-

sler et al. (1985) compared subsamples of the XBT data in the central Pacific and found that while the VOS network was barely adequate to resolve month to month fluctuations of the zonal geostrophic currents, it would not be able to meet the more stringent requirements of model verification for currents. McPhaden et al. (1988), using a linear, multimode model of wind-forced variability, estimated that dynamic height errors of about 2 dyn cm would result from the scatter of XBT profiles about the mean tracklines of the shipping routes. They also estimated that VOS XBT sampling would produce a signal/noise ratio (s/n) of about one for the annual and semiannual cycles of zonal geostrophic currents, and cautioned that higher frequencies would be poorly resolved. Hayes and McPhaden (1992) used Monte Carlo techniques to construct many realizations of monthly time series from buoy observations at 110° and 140°W on the equator. Their estimated s/n (defining the noise as the rms deviation between the subsampled and complete time series) were a function of longitude, depth, and frequency.

For many purposes we desire to map the quantity of interest. Optimal interpolation (OI) (Gandin 1963; Alaka and Elvander 1972) has been used to produce gridded maps of fields from irregularly sampled observations in numerous oceanographic situations (e.g., Bretherton et al. 1976; White and Bernstein 1979; Roemmich 1983). A principal advantage of OI is that, once the statistics of the field are known, the mapping skill of any sampling strategy can be estimated. Signal and noise variances and the spatial/temporal correlation structure are necessary inputs to an OI implementation, and the uncertainty of the resulting skill estimates are determined by the uncertainty of the values assumed for the parameters. For this reason, the estimation of these parameters from observations of the thermal field in the tropical Pacific has been the focus of several studies.

White et al. (1982) used the long record of annual cruises along 137°E from Japan to the equator, supplemented by mechanical bathythermograph profiles collected by Japanese fishing vessels in the western tropical Pacific, to estimate meridional scales from wave-number spectra and timescales from autocorrelation functions. These estimates were rather large (meridional scale of 600 km and timescale of 6 months); and this has been attributed to the dominance of variability due to El Niño events in the White et al. (1982) data. Meyers et al. (1991, hereafter MPSS) and Sprintall and Meyers (1991) used the VOS XBT dataset to produce estimates of the OI parameters for network design. The results suggested decorrelation scales of 3° latitude, 15° longitude, and 2 months, and signal/noise ratios close to or a little less than unity. They emphasized distinct differences in the space and time scale estimates for datasets that included or excluded the El Niños, particularly the very large event of 1982–83. A difficulty with this approach is that it is based on historical ship-

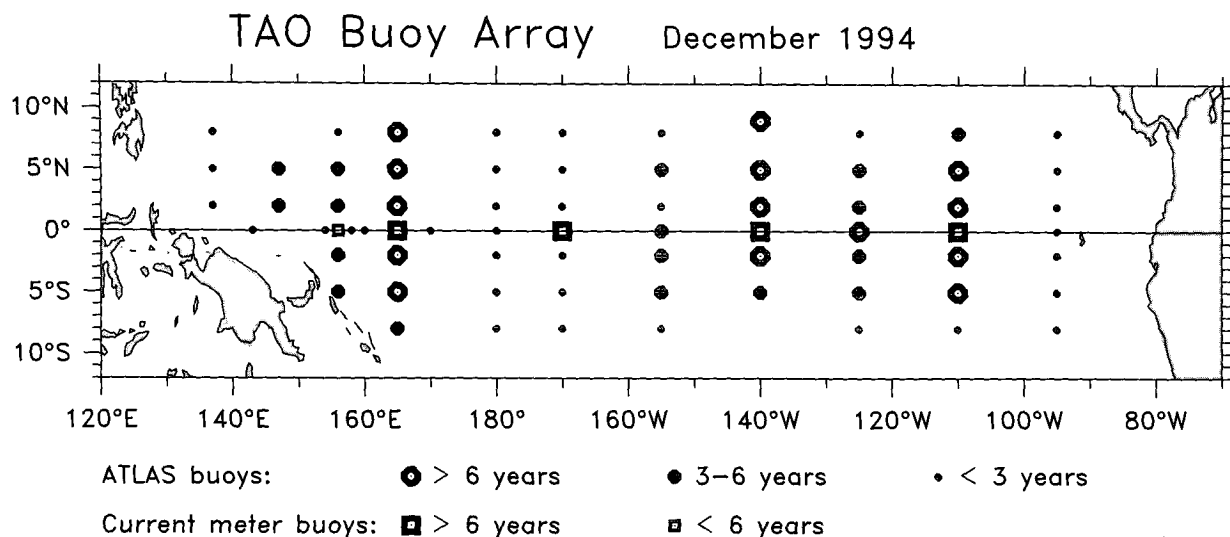


FIG. 1. Map of the TAO buoy network as of December 1994. The size of the symbol indicates how long a buoy has been in the water at that location. Round symbols show ATLAS thermistor chain buoys; squares show current meter buoys.

board data that is not adequate to fully resolve the broad spectrum of energy in the upper-ocean thermal field. This limits the ability to discriminate between different components of the low-frequency signal that may have quite different sampling requirements not well summarized by the single set of values used in OI.

The TAO array provides thermal data of unprecedented time resolution across the entire Pacific basin. For the first time it is possible to resolve all temporal variability on scales longer than a few minutes at some locations and longer than a day at all locations. Thus, it is now possible to compute temporal statistics for ocean thermal variability, whose errors are introduced primarily by the nonstationarity of the variability on the multiyear span of our records. As our records increase in length, we shall be able to examine the representativeness of results presented in this paper to longer time series and further diminish the uncertainties in these statistics. We are also able to estimate the spatial correlation statistics at a few locations with much greater confidence than has been possible and also distinguish spatial scales as a function of frequency. Now that the TAO array is fully deployed (McPhaden 1995), our ability to expand our knowledge of the spatial statistics will also increase greatly in the coming years.

The purpose of this paper is to present the time and space statistics of Pacific ocean thermal variability, as we are able to estimate them at this time from the TAO array, and to offer some discussion of the implications of these results for the effectiveness of the TPTMS as it is configured at present. As the TAO records grow in length we shall update and extend these statistics, as well as our assessment of the effectiveness of the TPTMS. Our analysis focuses on sea surface temper-

ature and depth of the 20°C isotherm (Z20). SST is the quantity through which the atmosphere responds to changes in the ocean, and it is crucial to understanding the coupled climate system. Z20 has been used in many studies as a proxy for the depth of the sharp thermocline in the tropical Pacific (Meyers 1979; Rebert et al. 1985; Kessler and Taft 1987). Much of the large-scale response of the ocean to wind fluctuations in this region is well-expressed in thermocline depth anomalies, particularly the propagation of equatorial waves. Since subsurface thermal variability in the tropical Pacific can often be characterized as vertical displacements of the entire upper layer, Z20 is a useful summary quantity.

2. The TOGA-TAO buoy array

The TOGA-TAO buoy array (Hayes et al. 1991a; McPhaden 1993) consists of nearly 70 deep-ocean moorings arranged in pickets nominally 15° longitude apart across the equatorial Pacific (Fig. 1). Most of these buoys are ATLAS thermistor chain moorings (Hayes et al. 1991a) that measure temperature at 1-m depth (taken here to be the SST) and ten subsurface depths down to 500 m, as well as near-surface winds, relative humidity, and air temperature. Subsurface instrument depths vary with location. Buoys in the western Pacific (west of 155°W) are instrumented at 25-m intervals from the surface to 150 m, then at 50-m intervals to 300 m, with a deep instrument at 500 m. Eastern Pacific buoys have instruments at 20-m intervals to 140 m, with deeper instruments at 180 m, 300 m, and 500 m. The purpose of denser sampling of the upper water column in the eastern Pacific is to better sample the shallower thermocline there. Along the dividing line at 155°W, the instrument depths were

changed from the eastern Pacific to the western Pacific configuration in 1992.

The sampling schemes on ATLAS moorings have evolved with time (Mangum et al. 1994). For the past several years, air temperature, sea surface and subsurface temperatures, and relative humidity have been sampled every 10 minutes, and averaged hourly. Laboratory bench tests showed that the ATLAS water temperature measuring pods have a thermal response time constant (*e*-folding time) of 31 minutes. Pre- and post-deployment calibration suggests that the accuracy of the ATLAS temperature pods is 0.1°C (Mangum et al. 1994). Winds (not considered in this study) are presently sampled at a rate of 2 Hz for 6 minutes centered at the top of each hour, then vector averaged. All these quantities are formed into daily averages that are telemetered in real time by Service Argos (for surface quantities both the daily average and the most recent hourly values are transmitted, but for subsurface temperature only the daily averages are available; see Mangum et al. 1994). The daily average values of SST and subsurface temperature used in this study, computed from 144 10-min samples each day, represent an essentially unaliased daily time series.

At the four current meter sites along the equator (156°E, 165°E, 140°W, and 110°W) the vertical and temporal resolution is enhanced. The 25-m spacing extends to 250 m in the western Pacific, with additional thermistors at 3 m, 10 m, 30 m, and 400 m. The current meter sites in the eastern Pacific have near-surface instruments at 10 m, 25 m, 35 m, 45 m, and 60 m, with 20-m sampling to 160 m. Additional depths were sampled for limited periods at other depths for specialized short-term program experiments (see Freitag et al. 1987; McPhaden and McCartney 1992; McCartney and McPhaden 1993). On the current meter moorings, subsurface temperatures are sampled typically every 15 minutes, with a thermal response time constant of 100 s for the VACMs (vector averaging current meters) (Levine 1981). However, in some cases 1-min data are available from temperature recorders with a 10-s time constant. Subsurface values from current meter moorings are not transmitted in real time, but are stored internally and are available when the mooring is recovered. Accuracy of temperature measurements from the current meter moorings ranges between 0.01° and 0.05°C, depending on instrument type.

For this study, 20°C depth was computed by linear interpolation of the buoy temperature profile. This interpolation was checked by preparing "mock TAO" profiles from more than 36 000 historical XBT profiles in the TAO region (Kessler 1990) and subsampling these in the vertical at the TAO standard depths. Vertical resolution of XBT profiles is 3–4 m, much finer than that of a typical TAO mooring. The mean difference between the true 20°C depth from the XBTs and that from the mock TAO profiles was about 0.19 m (mock TAO deeper), with rms difference about 3 m

(of marginal significance given the resolution of the XBT itself). In 18 cases (about 1 in 2000), linear interpolation of the mock TAO profiles produced 20°C depth discrepancies greater than 20 m; however, visual inspection of the profiles suggests that many of these large differences were due to questionable XBT values. The variance associated with linear interpolation was about one-third as large as the variance of Z20 at periods less than 1 day (see section 4). We conclude that the linear interpolation used here gives a reasonable estimate of 20°C depth from TAO observations and is unlikely to contaminate the statistics presented.

Timelines showing the period of time when observations of SST and Z20 are available at each mooring used in this study are given in Fig. 2. Z20 lies generally within the thermocline throughout the region (e.g., Fig. 3), surfacing briefly in the eastern Pacific during the SST minima of the La Niña cold periods of 1983 and 1988. Because of the linear interpolation it generally has a more complete time history than any individual subsurface temperature record. At 0°, 110°N the time series of temperature extends from early 1980 to the present, and long time series are also found along 140°W and 165°E (McPhaden and McCartney 1992; McCartney and McPhaden 1993); these locations form the backbone of the present study. However, at most sites the records are much shorter, reflecting the gradual growth of the buoy array (Figs. 1 and 2). In all, the database contains some 822 000 instrument-days of data (as of 1 May 1994 when 63 moorings were active). Large symbols in Fig. 1 and bold labels in Fig. 2 highlight locations with at least three years of data.

Although the primary ocean dataset from the TAO buoy network is near-real-time daily averages from ATLAS moorings, we take advantage of the substantial amount of internally recorded finer temporal resolution temperature data available at the current meter sites. In particular we use two 38-day records of subsurface temperatures sampled at 1-min intervals with fast-response thermistors, four records of up to 3½ years of 15-min subsurface VACM temperatures, and four records of up to 9 years of 2-h SST (Table 1). These closely resolved time series together with the daily-average data allow examination of virtually all scales of temporal variability between the Brunt–Väisälä frequency and the ENSO timescale.

3. Overview of space/time variability

In this section we briefly summarize the range of variability observed in the moored time series data, as background to the computation of signal-to-noise ratios and time/space scales presented in sections 4–6. Means and standard deviations computed for a common 6-yr period (1 May 1988 to 30 April 1994) illustrate many of the significant features of the upper-ocean thermal field in the equatorial Pacific (Fig. 3 and Table 2). Along the equator, the thermocline slopes down-

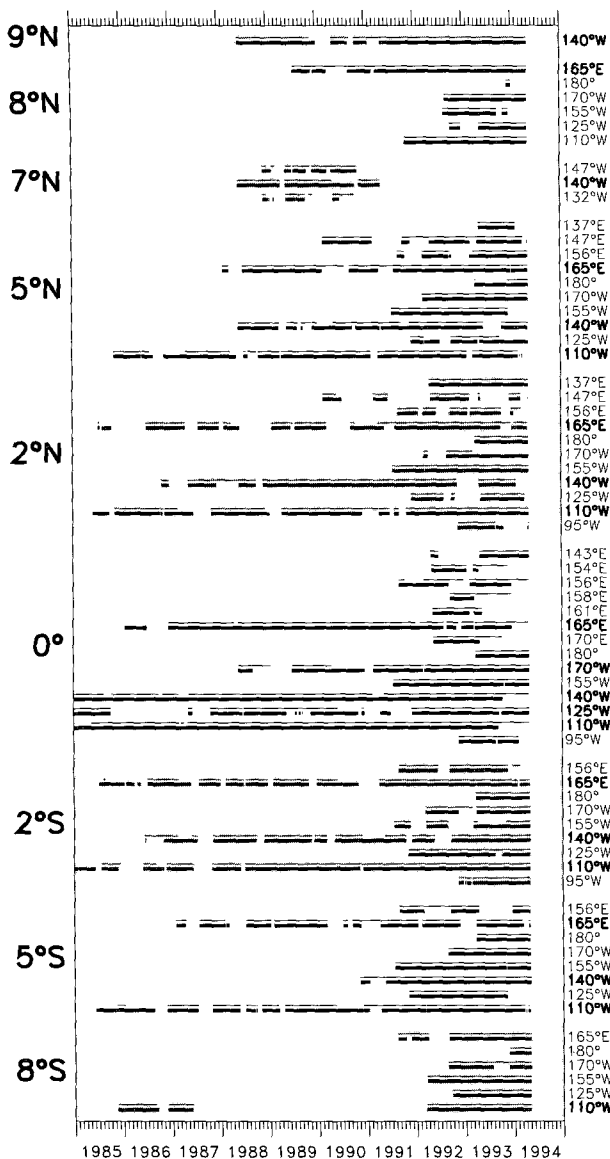


FIG. 2. Time history of sampling at all buoy locations. Each buoy is denoted by a thin line (for SST sampling) and a thick line (for Z20 sampling). Alternate shaded and white areas separate buoy latitudes. At a few locations along 110°W, 140°W, and 165°E, sampling began earlier than 1985 and is not shown.

ward to the west in response to trade-wind-driven westward mean currents that pile up warm surface-layer waters in the western Pacific (Fig. 3a). In the eastern Pacific, cold thermocline water from shallow depths is upwelled to the surface, creating an equatorial cold tongue with minimum temperatures near the equator (Fig. 3b). At and to the east of 110°W, the cold tongue exhibits a meridional asymmetry, with a bias toward colder temperatures in the Southern Hemisphere in response to pronounced southerly wind forcing. West of 140°W, the cold tongue progressively weakens as the

thermocline, which supplies the cold water to maintain it, deepens. Hence, west of the date line an equatorial minimum in SST is generally not evident; instead, SST in the western Pacific is characterized by a relatively homogeneous pool of warm water with temperatures greater than 28°C.

Meridional thermocline sections (Fig. 3b) show characteristic features associated with geostrophic zonal currents. For example, all three sections show spreading of the equatorial thermocline associated with the Equatorial Undercurrent, and downward sloping isotherms between 2°–5°N and 2°–5°S associated with the westward South Equatorial Current. Along 140°W and 165°E, the upward sloping isotherms poleward of 5°N indicate the presence of the eastward North Equatorial Countercurrent (NECC); this feature is missing in the 110°W section for lack of sufficient data at 8°N.

Variability about the mean tends to be highest in the upper thermocline and higher in the eastern Pacific than in the western Pacific. Interestingly, near-equatorial latitudes tend to be characterized by a local minimum in variability in the thermocline, whereas at the surface in the eastern Pacific, there is a local maximum in variability at the equator. To the extent that subsurface variability reflects in part vertical motion of the thermocline, the equatorial subsurface minimum may reflect the weakened mean gradient at the equator. The local equatorial maximum at the surface, on the other hand, could reflect that, compared to higher latitudes where SST is primarily determined by surface heat flux variations, there are a number of processes that affect SST in the equatorial cold tongue (cf. Hayes et al. 1991b; Chang 1993).

There is a broad spectrum of frequencies that contribute to the variability shown in Fig. 3, as illustrated in a few individual time series at 110°W, 140°W, and 165°E. An 8.5-yr segment of SST data at 110°W for example (top panel of Fig. 4a) shows a prominent seasonal cycle with peak-to-peak amplitude of about 5°C. Superimposed on this seasonal cycle are interannual variations associated with the 1986–87 ENSO and the 1988 La Niña. The temperature range is 12°C, with a minimum of about 17°C in late 1988 and maxima of about 29°C during ENSO events in 1987, 1992, and 1993. Note the extremely rapid warming (10°C in 2 months) that terminated the La Niña at the beginning of 1989 (McPhaden and Hayes 1990).

The middle panel of Fig. 4a shows SST on an expanded scale during 1990, which is a fairly normal year (i.e., a non-El Niño, non-La Niña year). The variability now visible is composed of one realization of the seasonal cycle plus a series of tropical instability waves (TIW) beginning in June. Each TIW appear as an abrupt 2°C pulse in the SST lasting perhaps 10 days, without a symmetric cold phase. It is clear from this figure that infrequent sampling, as for example from monthly VOS cruises, could distort estimates of the amplitude and phase of the seasonal cycle, since some

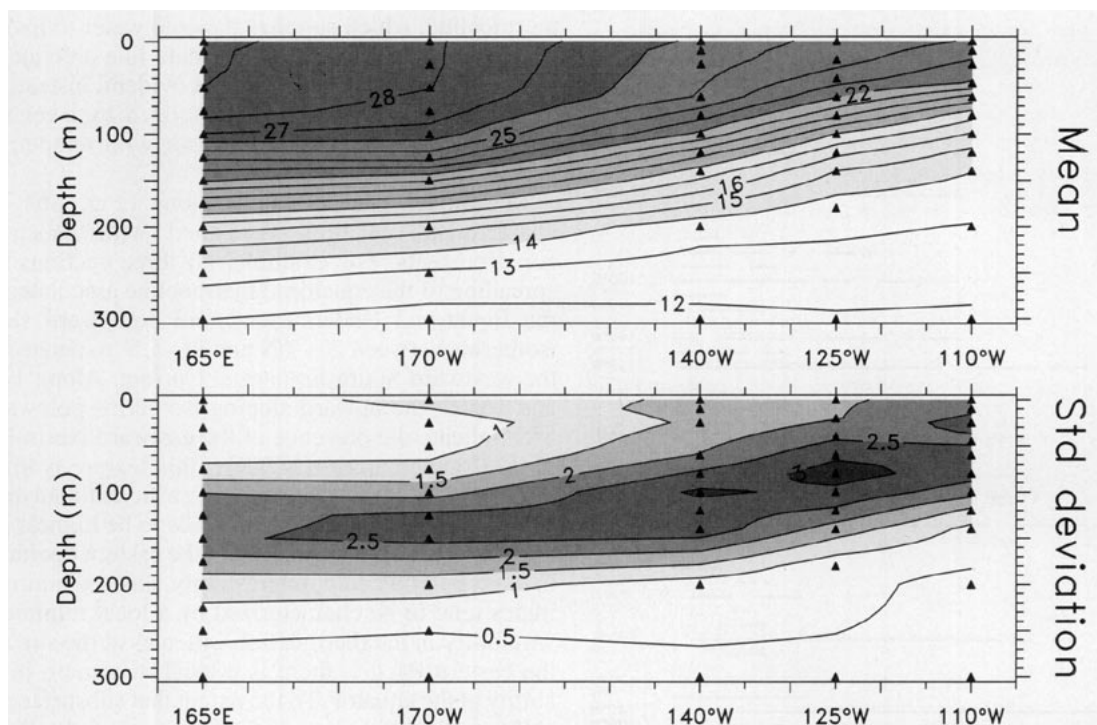


FIG. 3. (a) Mean and standard deviation of temperature along the equator for the period May 1988 through April 1994, linearly interpolated between the moorings. Black triangles show instrument locations. Contours of mean temperature are given every 1°C . Contours of standard deviation are given every 0.5°C . Dark shading shows high values.

samples in the second (cool) half of the year might measure the SST during a TIW pulse. The two panels at the bottom of Fig. 4a show further detail from the months of May (during the warm phase of the seasonal cycle) and October 1990 (during the cold phase of the seasonal cycle). Variability during May 1990 exhibited weekly timescale fluctuations of about 1°C peak to peak and a fairly regular diurnal cycle with a range at times of 0.6°C . This diurnal variability was nonsinusoidal, with sharp warming in the late morning and early afternoon, followed by a more gradual cooling. Spectrally, this nonsinusoidal diurnal cycle will produce a number of harmonics of the daily period in the frequency spectrum (e.g., Fig. A2). During October 1990, the diurnal cycle was somewhat weaker, possibly due to stronger easterlies and associated enhanced turbulent mixing in the surface layer at this time of year (Taft and McPhaden 1990). The October segment also shows in detail the evolution of one cycle of a TIW warming. These time series can be contrasted with the SST at 165°E (Fig. 4b). In the western Pacific, mean temperatures are higher, but the temperature range, as well as the amplitude of interannual variations and seasonal cycle, are much smaller (see also Table 2). Moreover, in the western Pacific, the seasonal cycle is characterized more by a two cycle per year variation rather than a one cycle per year variation as in the eastern

Pacific (e.g., McCarty and McPhaden 1993). Instability waves are not prominent at 165°E . The diurnal cycle, on the other hand, is as energetic as lower-frequency variations. Thus, infrequent sampling could lead to significant aliasing of the diurnal cycle into lower frequencies of more direct climatic interest at 165°E .

The 20°C isotherm depth time series at 0° , 140°W is shown in Fig. 4c. The annual cycle is less visually prominent in Z20 than in SST at this location, whereas signals associated with the ENSO cycle in 1986–88 are very pronounced. The middle panel shows the year 1991 in detail. Superimposed on the annual cycle, which had a range of about 80 m in 1991, are 2–3 month-period intraseasonal Kelvin waves with peak-to-peak amplitudes of 20–40 m (Kessler et al. 1995). The highest resolution 1-min data in the lower two panels of Fig. 4c (November and December 1991) exhibit primarily semidiurnal tidal fluctuations. These fluctuations are nonstationary, with peak-to-peak amplitudes of up to 30 m on some days, while being nearly absent on others.

4. Signal/noise ratios

A convenient description of the error structure associated with sampling strategies is given by the pa-

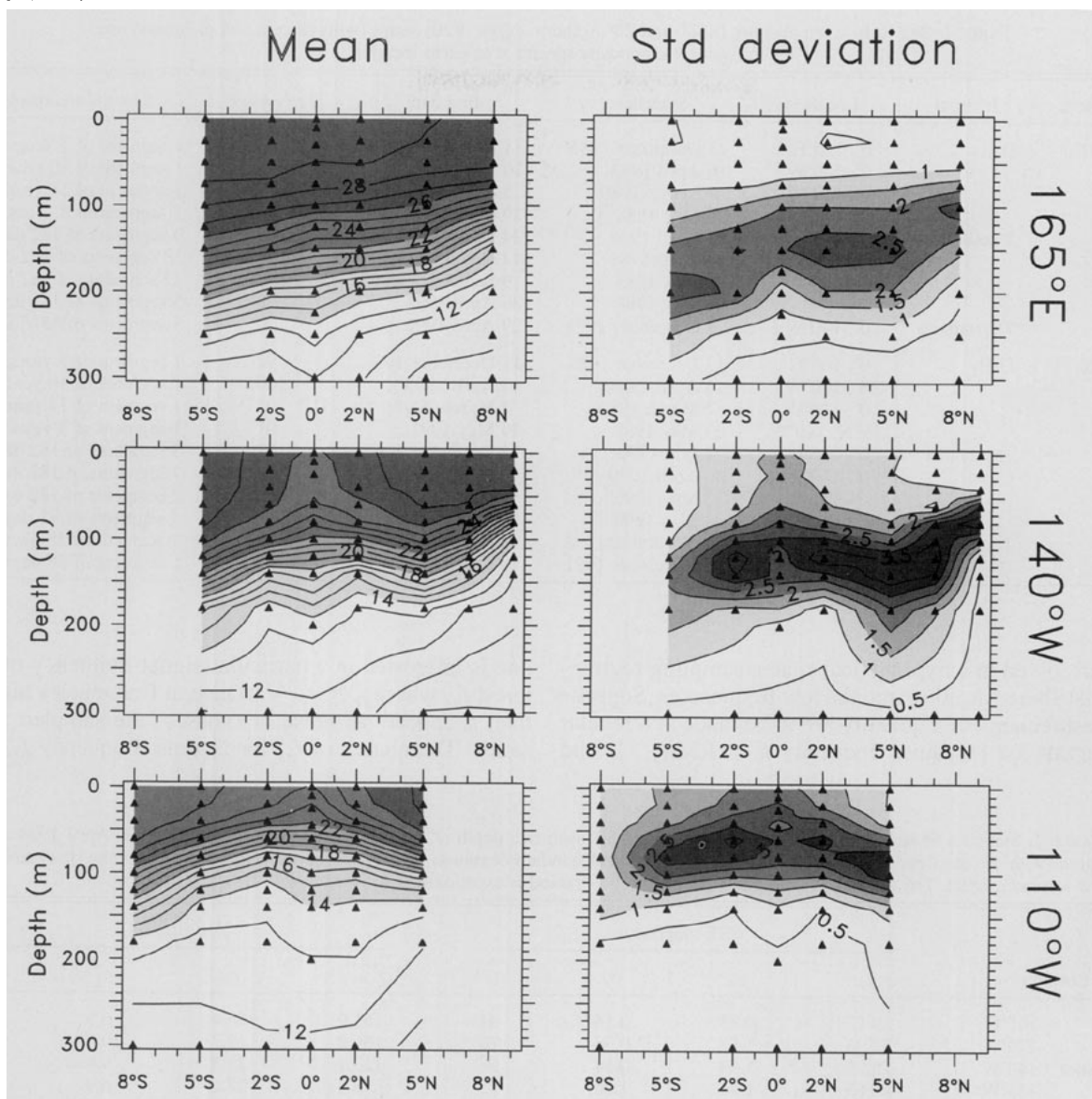


FIG. 3. (Continued) (b) As in (a) but meridional sections along 165°E, 140°W, and 110°W.

rameters signal (s) and noise (n) variance and the signal to noise ratio (λ), defined as follows. The total variance σ^2 of an observed quantity is the sum of signal and noise variance: $\sigma^2 = s + n$. The noise variance represents unresolved variability with scales smaller than the time and distance between observations (geophysical noise). We assume that instrument noise is negligible from the TAO moorings (see section 2). The signal to noise ratio λ is then defined as the rms measure: $\lambda = (s/n)^{1/2}$.

In many studies, λ has been estimated from observations as a overall measure that characterizes a sampling regime and dataset; for a given geophysical quantity in a particular region, λ is a function of the sample rate. The present study takes advantage of the finely

resolved TAO buoy time series to delineate exactly how high-frequency variability would produce aliasing in various hypothetical sampling regimes. We expect the signal to noise ratio to vary with the sampling rate, but we expect it to also depend on the investigator's choice of low-frequency signal that is to be observed. Thus, we will examine the variation of a generalized λ as a function both of the sampling and of the frequency of interest. The results are designed to permit the tailoring of a sampling strategy by choosing a sample rate that produces the desired signal to noise ratio given a particular signal frequency of interest.

The frequency dependence of the signal to noise ratio can be studied through spectrum folding, which shows how each element of high-frequency variability

TABLE 1. Sea surface temperature (SST) and 20° isotherm depth (Z20) series (with percent completeness) used to compute composite spectra at selected locations.

Variable	Interval	Location	Start date	End date	Percentage	Spectral treatment
SST	Daily	0°, 165°E	13 December 1986	11 December 1993	95	1 segment of 7 years
		0°, 140°W	16 April 1983	10 April 1993	81	1 segment of 10 years
		0°, 110°W	7 March 1980	5 March 1994	83	1 segment of 14 years
		7°N, 140°W	29 May 1988	29 May 1991	76	1 segment of 3 years
	2 hour	0°, 165°E	20 April 1986	24 December 1993	63	9 segments of 182 days
		0°, 140°W	27 April 1984	12 October 1993	90	18 segments of 182 days
		0°, 110°W	9 May 1985	9 September 1993	100	17 segments of 182 days
		7°N, 140°W	28 May 1988	30 April 1991	78	5 segments of 182 days
	7½-minute	0°, 140°W	9 November 1991	29 April 1992	100	5 segments of 45½ days
Z20	Daily	0°, 165°E	13 December 1986	11 December 1993	97	1 segment of 7 years
		0°, 140°W	16 April 1983	10 April 1993	100	1 segment of 10 years
		0°, 110°W	7 March 1980	5 March 1994	94	1 segment of 14 years
		7°N, 140°W	29 May 1988	29 May 1991	91	1 segment of 3 years
	15 minute	0°, 165°E	1 July 1990	24 December 1993	81	5 segments of 182 days
		0°, 140°W	30 April 1990	12 October 1993	100	7 segments of 182 days
		0°, 110°W	15 May 1990	9 September 1993	100	7 segments of 182 days
		7°N, 140°W	4 May 1990	30 April 1991	92	4 segments of 91 days
	1 minute	0°, 156°E	5 November 1992	13 December 1992	100	1 segment of 38 days
		0°, 140°W	9 November 1991	18 December 1991	100	1 segment of 38 days

(unresolved in a hypothetical coarse sampling regime) is distributed as noise into the low frequencies. Suppose measurements of a quantity are to be made at a regular intervals Δt [Nyquist frequency $f_0 = (2\Delta t)^{-1}$], and

one is interested in a particular signal frequency of interest f_p , where $f_p < f_0$. Variance at frequencies higher than f_0 appears as noise in (aliases) the sampled time series. The aliases of f_p , for Nyquist frequency f_0 , are

TABLE 2. Statistics of sea surface temperature (SST) and 20° isotherm depth (Z20) for the period 1 May 1988 to 30 April 1994 at the locations with the most complete records. The overall mean and standard deviation are μ_0 and σ_0 , respectively, and σ_s is the rms amplitude of the seasonal signal. The fraction of data available for the 6-yr period is expressed as a percentage.

		SST (degrees)				Z20 (meters)			
Location		μ_0	σ_0	σ_s	(%)	μ_0	σ_0	σ_s	(%)
Equator	165°E	29.27	0.73	0.14	94	161.9	18.4	6.3	91
	170°W	28.03	1.17	0.34	76	156.3	17.7	10.5	82
	140°W	25.79	1.59	0.54	96	113.1	27.3	9.8	91
	125°W	24.63	1.94	1.06	75	78.3	28.1	6.9	76
	110°W	23.91	2.20	1.50	99	56.3	25.6	6.8	86
165°E	8°N	28.79	0.74	0.61	79	116.7	14.7	—	70
	5°N	29.05	0.54	0.33	94	152.4	19.0	—	82
	2°N	29.33	0.57	0.23	69	161.6	19.3	—	70
	0°	29.27	0.73	0.14	94	161.9	18.4	6.3	91
	2°S	29.38	0.64	0.18	78	174.9	17.5	5.4	85
	5°S	29.52	0.49	0.19	79	193.4	20.7	—	73
140°W	9°N	27.65	0.83	0.61	88	75.3	12.7	5.0	86
	7°N	27.36	0.67	—	38	112.5	26.5	—	46
	5°N	27.50	1.07	0.52	80	134.4	23.3	15.7	84
	2°N	26.80	1.31	0.51	80	115.9	22.4	13.5	84
	0°	25.79	1.59	0.54	96	113.1	27.3	9.8	91
	2°S	26.54	1.35	0.62	78	122.1	21.8	11.8	85
	5°S	27.69	0.80	—	57	156.1	16.2	—	52
110°W	5°N	27.23	0.98	0.70	87	91.1	17.6	12.5	86
	2°N	25.84	1.77	1.13	88	66.5	18.8	7.8	85
	0°	23.91	2.20	1.50	99	56.3	25.6	6.8	86
	2°S	24.55	2.01	1.73	97	60.2	21.1	5.5	96
	5°S	25.24	1.58	1.45	82	80.6	18.7	8.6	87
	8°S	25.94	1.23	—	35	114.6	9.8	—	35

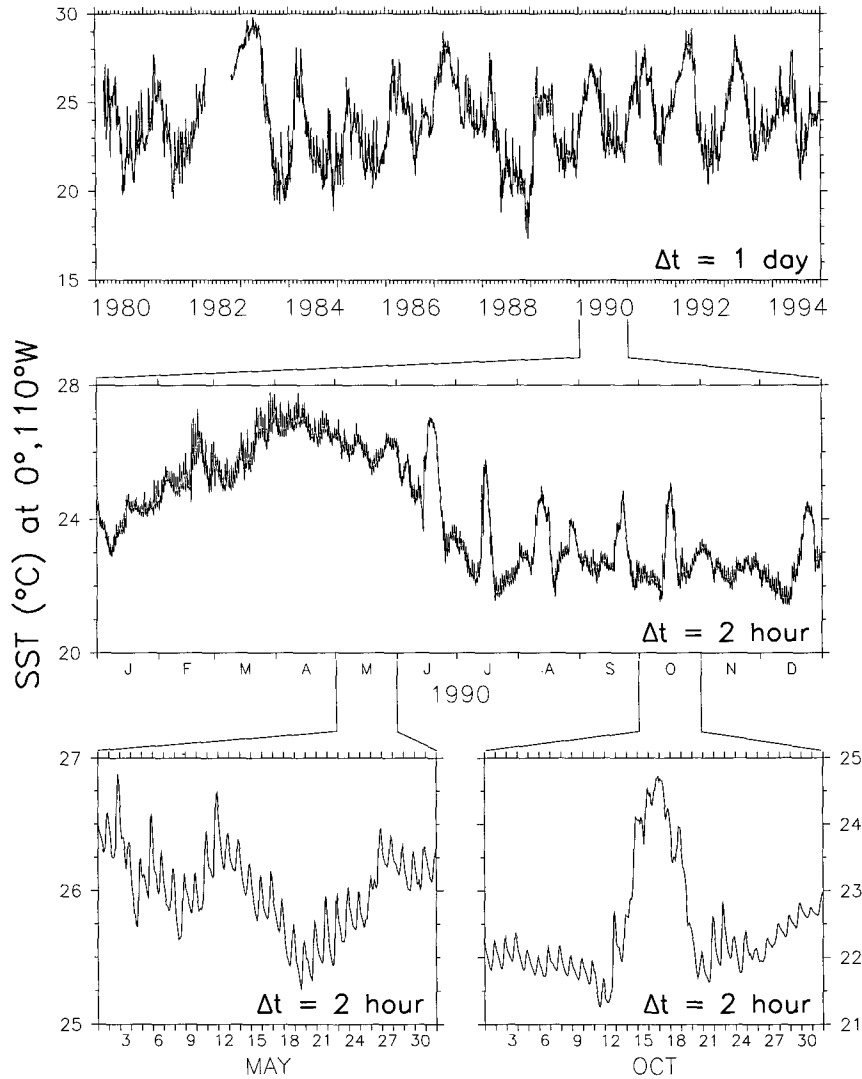


FIG. 4. (a) Time series of SST observations at 0° , 110°W from daily and 2-h sampling, as indicated. Top: the entire 15-yr time series. Middle: the year 1990 on an expanded scale. Bottom: the months April and October 1990 on an expanded scale. The temperature scale differs among the panels as indicated in the ordinate axis labels.

the frequencies that repeat the same point in the sinusoidal components when sampled at rate Δt , and these are $f = 2kf_0 \pm f_p$ for $k = 1, 2, 3, \dots$. If the fully resolved time series has spectrum $S(f)$, then the noise is

$$N(f_p, f_0) = \sum_{k=1}^{\infty} S(2kf_0 \pm f_p), \quad (1)$$

which is a function both of the sampling and of the frequency of interest. This is called spectrum folding because it can be visualized as folding the spectrum (drawn on paper with a linear frequency axis) into an accordion shape with alternating folds at each kf_0 ; then f_p and all its aliases will be lined up. Spectrum folding maps each element of noise [$S(f)$ for $f > f_0$] onto a

particular low frequency $f_p < f_0$. The spectral density at frequency f_p that would be measured given sample rate $(2f_0)^{-1}$ is $\hat{S}(f_p, f_0) = S(f_p) + N(f_p, f_0)$. Here, where we assume that all significant high-frequency variability is resolved by the buoys ($f_0 \rightarrow \infty$), the signal variance at f_p is just the spectrum value $S(f_p)$, so the ratio of the signal (at frequency f_p) to the noise due to sampling at rate $f_0 = 1/2\Delta t$ is

$$\Lambda(f_p, f_0) = \sqrt{S(f_p)/N(f_p, f_0)}, \quad (2)$$

where, as in Eq. (1), we use the uppercase symbols $S(f)$, $N(f_p, f_0)$, and $\Lambda(f_p, f_0)$ to indicate the frequency-dependent analogues of s , n , and λ . The original parameters s and n are the integrals of $S(f)$ from 0 to f_0

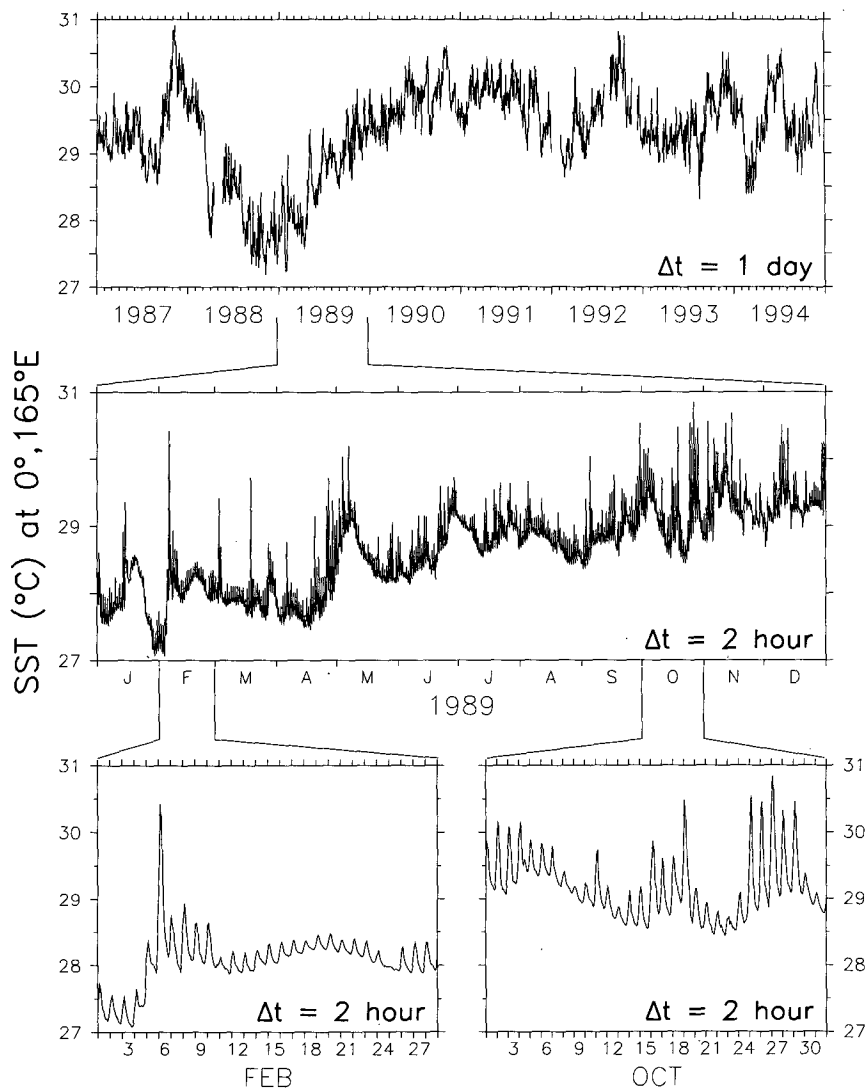


FIG. 4. (Continued) (b) As in (a) but for SST at 0°, 165°E.

and from f_0 to ∞ , respectively. Equation (1) shows that n can also be written as the integral of $N(f_p, f_0)$ over all f_p (recall that $0 < f_p < f_0$)

$$n(f_0) = \int_{f_0}^{\infty} S(f) df = \int_0^{f_0} N(f_p, f_0) df_p, \quad (3)$$

which confirms that the total noise (the integral over the unresolved high frequencies) equals the total aliasing integrated over the low frequencies. Compared to n , which is a function of the sample rate only, $N(f_p, f_0)$ gives additional detail indicating the error in the signal estimate at each f_p due to high-frequency aliasing. Strictly, the analogy with parameters used by MPSS and others is imprecise because of the additional effect of data binning, in which MPSS assume that each bin is oversampled, such that signal and noise in the

frequency range between f_0 and the bin scale are averaged out. In that case, the total noise [first integral of (3)] is larger than the total aliasing [second integral of (3) with an upper integration limit at the bin frequency]. Therefore, although where possible we quantitatively compare our results with signal and noise values reported by MPSS, it should be recognized that this is only an approximate comparison.

Formally, calculating the sum in (1) requires that the full spectrum $S(f)$ be known, which of course it never is. However, the time series listed in Table 1 (with sampling as fast as once per minute) can be used to describe a very large fraction of the high-frequency variance. The time series at 110°W, 140°W, and 165°E on the equator and at 7°N, 140°W were used to construct spectra of SST and Z20 extending over as much as six decades of frequency, by patching together spec-

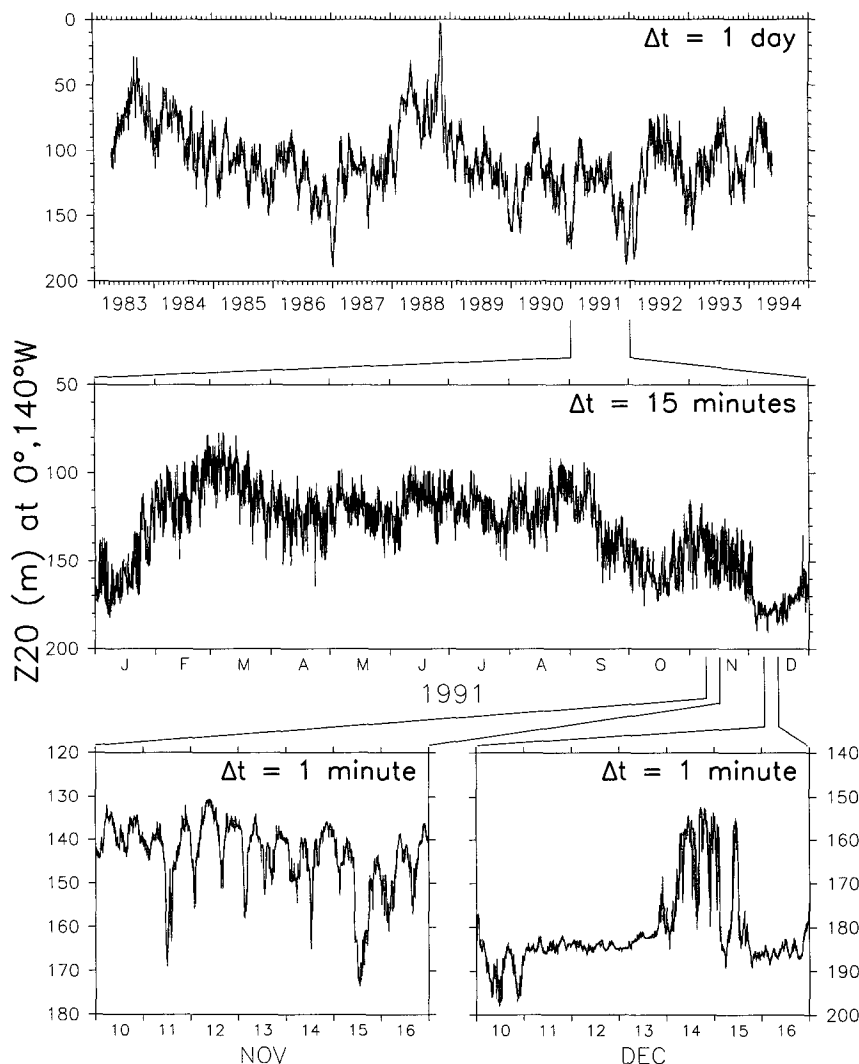


FIG. 4. (Continued) (c) As in (a) but for Z20 at 0°, 140°W, based on daily, 15-min and 1-min sampling.

tra constructed from decade-long time series of daily data with the various-length time series of higher temporal resolution. These composite spectra are shown in Fig. 5a for SST and Fig. 5b for Z20. In Figs. 5a and 5b, the overlap among the spectra is omitted for clarity, but the three spectra forming the composites at each location agree reasonably well in the overlap region. The composite spectra follow a roughly -1.5 power dependence over their entire range. The semidiurnal tide is a prominent mode of high-frequency variability in Z20, the spectrum of which otherwise tends to fall off at a fairly regular rate (Fig. 5b). There is some suggestion (most clearly at 165°E) of an increase of Z20 variability near the Väisälä frequency, which has periods near 5–10 min (150–300 cpd) for the central thermocline region. Harmonics of the diurnal frequency form prominent peaks in the SST spectra at all

four locations (Fig. 5a), due to the nonsinusoidal shape of the daily cycle (e.g., Fig. 4a). The slopes of the SST spectra are generally slightly steeper than those for Z20.

The results of the spectrum folding calculation [the rms signal/noise ratio $\Lambda(f_p, f_0)$ given by Eq. (2)] using the composite spectra are contoured in Fig. 6 for SST and Z20 at 0°, 110°W and 0°, 165°E to represent the east and west Pacific. Here Λ is shown as a function of both sample rate and of frequency of interest. As would be expected, it is larger for short sampling intervals or low frequency of interest. For example, if an investigator had time series of Z20 at 0°, 110°W sampled every 30 days, Fig. 6 (top right) shows that the annual cycle would be expected to have Λ of about 3, and the ratio would be less than 1 for signals with periods shorter than 75 days. Alternatively, one might be plan-

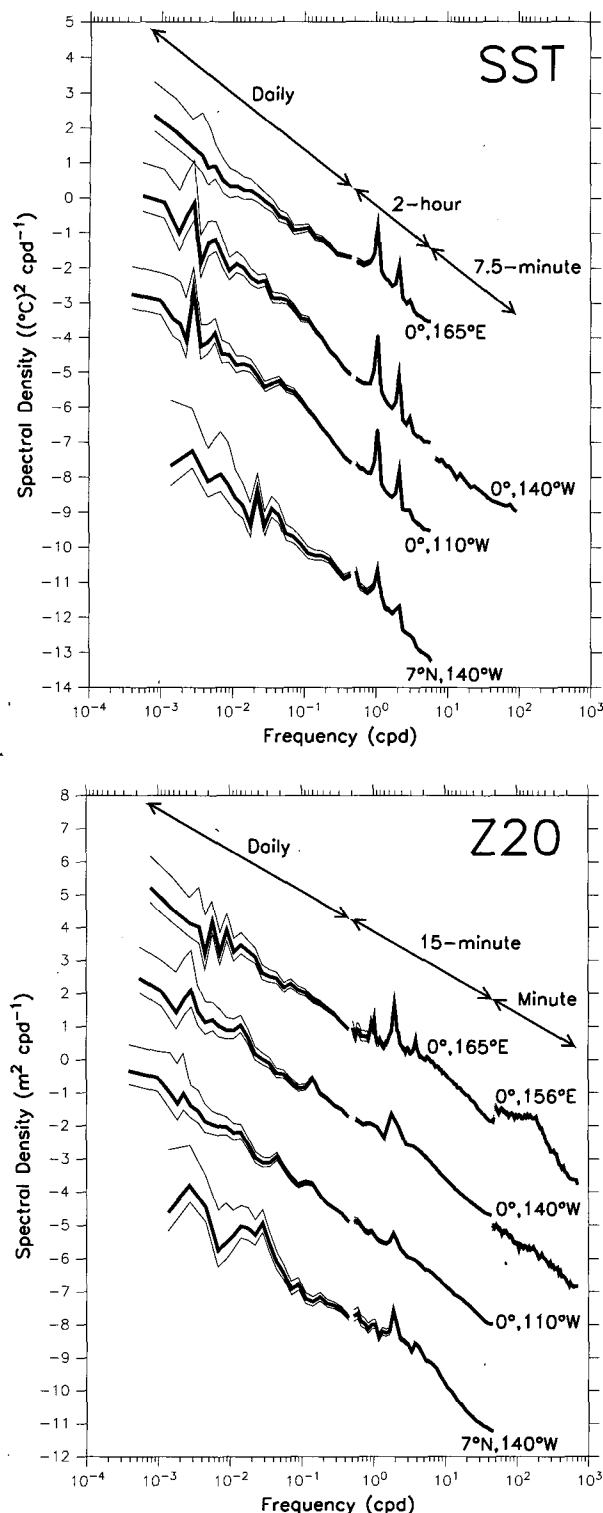


FIG. 5. (a) Composite spectra of SST at the equator, 110°W, 140°W, and 165°E, and at 7°N, 140°W, using data described in Table 1. The ordinate scale is correct for the top spectrum, while the other locations are shifted down three decades each; ordinate axis values are shown just as powers of 10. At 0°, 140°W the composite is composed of daily, 2-h, and 7½-min data; at the other locations only

ning an experiment to study the intraseasonal Kelvin waves (periods about 60 days) and seek a sampling strategy that gave $\Lambda = 2$ for Z20; Fig. 6 (right panels) suggests that sampling every 7 days would be required in either location.

A comparison between values of Λ in the east and west Pacific is given in Fig. 7, in which the results have been band-averaged into three commonly studied frequency ranges of interest [interannual, the annual cycle, and intraseasonal (defined as periods of 30–100 days)]. This comparison shows that, overall, sampling requirements are less stringent in the east because the signals there are larger in all three bands (Fig. 3). MPSS found a similar result. If we take $\Lambda = 2$ as an (admittedly somewhat arbitrary) standard, then Fig. 7 suggests that, for interannual-band SST, sampling at roughly 100-day intervals is sufficient both in the east and the west. Interannual Z20 at 110°W would also be adequately sampled at this rate, but for Z20 at 165°E one must sample every 40 days to reach the $\Lambda = 2$ standard. For the seasonal cycle of SST, 100-day sampling suffices at 110°W, but 20-day sampling is needed at 165°E; seasonal Z20 requires 20–30-day sampling at both locations. VOS XBT sampling, at a nominal rate of 20–30-day intervals, approaches the $\Lambda = 2$ standard for all of these low-frequency quantities, but barely reaches $\Lambda = 1$ for the intraseasonal band of either SST or Z20 at either location.

For a spectrum $S(f)$ that follows an inverse power law dependence [$S(f) = f^{-a}$, for $a > 1$], it can be shown that the sum $N(f_p, f_0)$ becomes increasingly white with respect to f_p for low values of a and thus is largely a function of sample rate alone (see appendix). The spectra of temperature in the equatorial Pacific vary roughly like $f^{-1.5}$ over a wide frequency range (e.g., Fig. 5), so the aliased noise tends to be evenly distributed over all the low frequencies and $N(f_p, f_0)$ is approximately a function of sampling Nyquist frequency f_0 alone. Figure 8a shows the integrated noise variance $n(f_0)$, calculated from the first of equations (3), for SST and Z20 at four selected locations with long records of high-resolution data. Rms Z20 noise levels are about 4–6 m for daily sampling, then rise to 8–15 m for 30-day sampling, while for SST the corresponding levels are 0.1°–0.2°C and 0.3°–0.7°C. For both SST and Z20, the noise variance increases by about a factor of 10 as the sample rate decreases from daily to 100-day sampling. SST noise varies by as much as a factor of 10 among the four locations studied,

daily and 2-h data are available. The breaks in the spectra separate the differently sampled datasets (for clarity the overlap in the spectra is not shown). Thin lines indicate the 95% confidence intervals. (b) As in (a) but for Z20. The three sampling regimes are daily, 15 min, and 1 min (only at 0°, 140°W and 0°, 156°E). The short record of 1-min data at 0°, 156°E is used to extend the spectrum at 0°, 165°E.

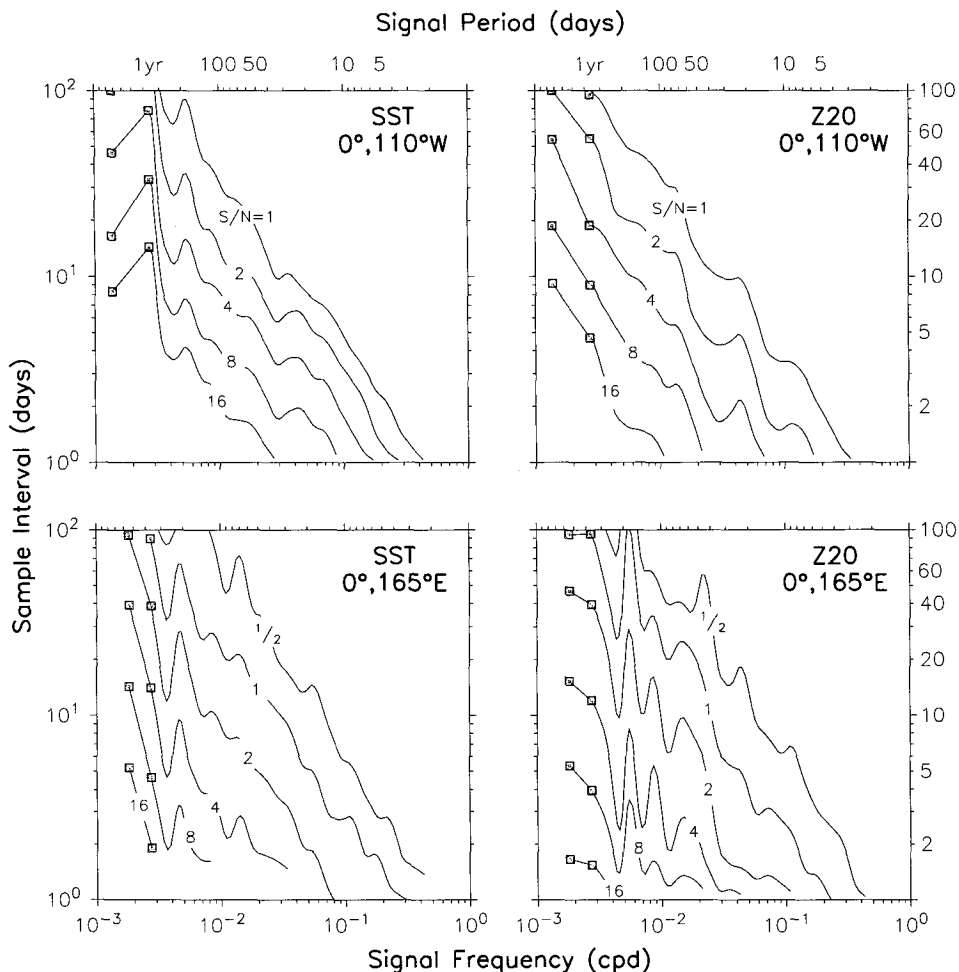


FIG. 6. Signal to noise ratios for SST and Z20 at 0° , 110°W and 0° , 165°E , as a function of signal frequency (cycle/day) (abscissa) and sampling interval (days) (ordinate). Values are Λ given by Eq. (2). Black squares indicate Λ averaged in the annual and interannual bands.

but Z20 noise variance is much more consistent over the region. The values shown in Fig. 8a can be used to estimate the expected signal/noise ratio for planning or monitoring purposes, if one knows or can estimate the amplitude of the signal of interest. The even distribution of noise over the low frequencies is also the reason that the Λ contours shown in Fig. 6 appear roughly parallel.

As we have noted, the signal/noise ratio Λ is a measure of the aliasing at a particular signal frequency and so is not directly comparable to λ used by MPSS, which is an overall measure depending only on the sampling rate. Optimal interpolation also requires a global estimate of λ that characterizes a dataset. However, the composite spectra (Fig. 5) can be used to find an overall signal/noise ratio corresponding to λ by integrating the spectrum. The noise is given by (3) (shown in Fig. 8a) and the signal is the integral of all the remaining lower-frequency spectrum; therefore, total observed

variance is the sum of signal and noise. Since the buoy time series only resolve the signal to maximum periods of a few years, these values represent daily to interannual variability. The ratio $(s/n)^{1/2}$ calculated from the integrated spectra is a function only of Nyquist frequency f_0 and is roughly comparable to the values computed by MPSS, which they found by extrapolation of autocorrelation functions based on VOS data; it is shown in Fig. 8b. These overall signal/noise ratios increase from about unity for 100-day sampling to about 5 for daily sampling and are somewhat higher for SST than for Z20 (Fig. 8b).

Numerical values of $(s/n)^{1/2}$ from the integrated spectra are given in Table 3 for 30-day sampling regimes, as is typical of the VOS dataset, along with the corresponding values from MPSS (their Tables 1 and 2, and their Fig. 3). Overall signal/noise ratios in this range are typically 2–3 for SST and about 2 for Z20, considerably higher than those reported by MPSS, which were usually

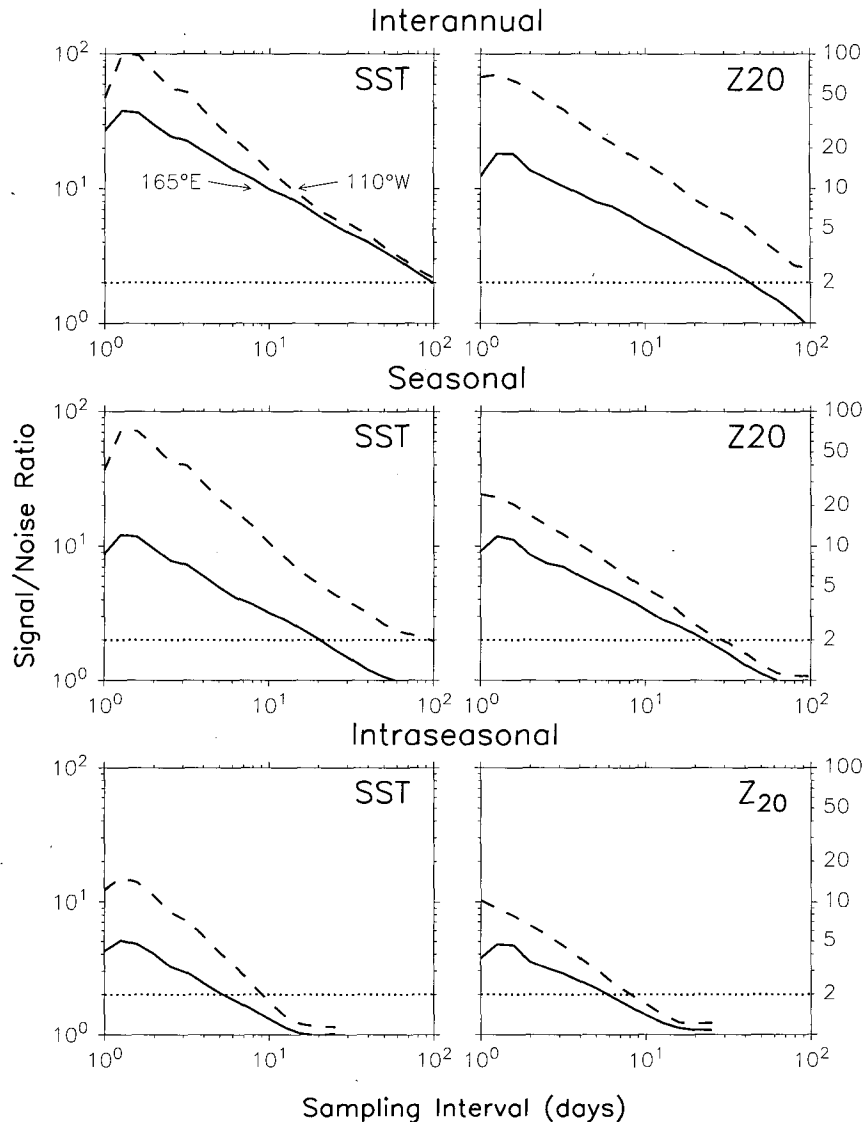


FIG. 7. Signal to noise ratios (Λ) for SST and Z20 at 0° , 110°W and 0° , 165°E averaged into three frequency bands and plotted as a function of sampling interval. These are vertical cuts through the contoured values of Fig. 6. The solid line indicates 165°E and the dashed line 110°W . The dotted horizontal line indicates the value $\Lambda = 2$, taken as a desirable target for sampling.

less than 1 for their non-ENSO period and up to 2 when the large 1982–83 El Niño event was included. We will discuss reasons for this discrepancy in section 7.

5. Timescales

The buoy time series can also be used to estimate time scales in frequency partitions by filtering the data and examining the autocorrelation functions (ACFs). MPSS estimated temporal decorrelation scales from ACFs of the space and time binned VOS time series used in the estimation of signal and noise variance. The present study extends those findings by using the bet-

ter-resolved buoy time series, which allows the stratification of results by frequency. We estimated the timescale as the integral to the first zero-crossing of the ACF (Stammer and Boning 1992). MPSS defined the decorrelation timescale as either as the first zero-crossing of the ACF for oscillatory processes or as the e -folding scale of a fitted Gaussian function otherwise. Our definition produces values somewhat shorter than those of MPSS (in the case of a perfectly sinusoidal ACF, our integral definition gives the timescale as the period divided by 2π , whereas MPSS's definition would give the period divided by 4). Three versions of the dataset were studied: first, the unfiltered, detrended time se-

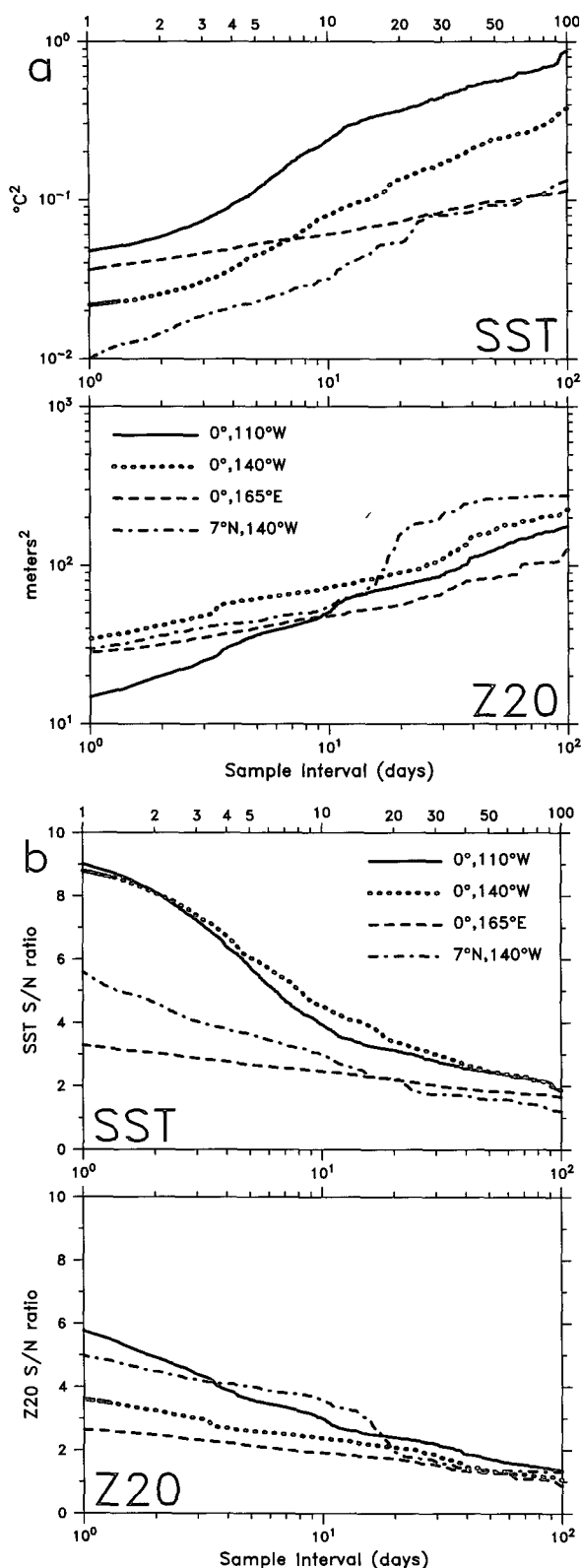


FIG. 8. (a) Noise variance as a function of sample rate at the equator, 110°W , 140°W , and 165°E , and at 7°N , 140°W . The noise is estimated from the spectra shown in Fig. 5, using Eq. (3), summed

ries; second, the time series with the seasonal cycle (1, 2, 3 cpy harmonics) removed, then low passed with half-power at 150-day periods; and third, a high-passed version of the time series obtained by removing the seasonal cycle as well as the low-passed time series variations. Only daily average data have been used in these calculations.

Figure 9 is an example of the ACFs found from these three dataset versions for the 14-yr record of SST at 0° , 110°W . The ACF from unfiltered data represents principally the annual cycle, while the ACF from low-passed data shows essentially the 4–5-year separation of the three ENSO events (1982, 1987, 1991) in this time series. The ACF from the high-passed time series falls to zero in less than 1 month, then oscillates around zero, with a period of about 2 months (Fig. 9). The resulting timescale estimates for SST at 0° , 110°W are 57 days ($0.98 \text{ yr}/2\pi$) for the unfiltered data, 105 days for the low-passed data, and 4.0 days for the high-passed data. Figure 10 summarizes the timescales for SST and Z20 at each buoy for both the low- and high-passed datasets. The low-passed timescales are typically 100 days or more for both SST and Z20, indicating low-frequency ENSO variations. Perhaps more surprising are the timescales for the high-passed data, which are about 4–6 days for both SST and Z20 everywhere in the TAO region (Fig. 10). The processes that produce variability of these quantities at periods less than 150 days are diverse, including tropical instability waves in the east Pacific SST north of the equator (Hansen and Paul 1984; Pullen et al. 1987; Halpern et al. 1988), intraseasonal Kelvin waves for equatorial Z20 (Kessler et al. 1995), other short-period equatorial waves (Wunsch and Gill 1976; Eriksen 1982; Weisberg and Horgan 1981), and synoptic weather disturbances, so it is not at all obvious why the timescales should be so homogeneous.

6. Space scales

a. Scale estimation method

The horizontal spatial scales of the thermal variability in the tropical Pacific have been estimated in numerous studies, often for the purposes of designing a sampling strategy (Barnett and Patzert 1980; White et al. 1982), or for optimal interpolation, where the spa-

over all possible frequencies from the highest to the value on the abscissa (see text). Top panel shows SST and bottom panel shows Z20. The location legend for both is in the lower panel. (b) Overall signal to noise ratio as a function of sample rate at the same locations as in (a), calculated by partitioning the spectra in Fig. 5 into noise [(a)] and signal (all remaining variance at periods up to 3 yr). The ratio is plotted as a function of the dividing frequency (axis labels show the equivalent sample rate). These values would be used to characterize a sampling regime for optimal interpolation. The location legend for both is in the upper panel.

TABLE 3. Overall signal/noise ratios calculated from integrated buoy spectra for the periods up to one cycle per $3\frac{1}{2}$ years, assuming 30-day sampling. The first column shows values using the full dataset; the next for the dataset with the annual cycle (three harmonics) removed; and the next for spectra truncated at 400-day periods. The final two columns show signal/noise ratios from Meyers et al. (1991), for non-ENSO periods, and overall. The overall values are in parentheses since these were estimated from Fig. 3 of Meyers et al. (1991).

Dataset	Full data	Annual cycle removed	400-day cutoff	MPSS (XBT)	
				Non-ENSO	Overall
SST					
0°, 110°W	2.79	1.79	2.37	1.6	(2.5)
0°, 140°W	3.01	2.56	2.00	0.7	(1.1)
0°, 165°E	2.04	2.00	0.88	0.5	(1.4)
7°N, 140°W	1.74	1.02	1.60	0.8	(0.9)
Z20					
0°, 110°W	2.18	2.13	1.34	0.9	(2.5)
0°, 140°W	1.82	1.60	1.41	0.5	(1.2)
0°, 165°E	1.53	1.31	1.10	0.5	(1.3)
7°N, 140°W	1.59	0.96	1.52	0.7	(2.4)

tial scales are parameters of analytic functions approximating an observed autocorrelation structure (Roemich 1982; Sprintall and Meyers 1991; MPSS; White et al. 1982).

In the present study, we make estimates of the zonal and meridional scales of SST and Z20 variability for comparison with previous estimates based on ship-board data. While the coarse spatial distribution of the TAO array renders it less suited for space scale determination than for time scales, the ability to preprocess the data into the seasonal cycle, and low- and high-passed versions of the time series allow for further insight and stratification of scale estimates by frequency. As in the case of the timescale estimates (section 5), space scales are found for three dataset versions: the unfiltered time series, the low-passed series with the seasonal cycle removed, and the high-passed time series. As was done for the timescales discussed in section 5, only daily averaged data were used.

Spatial lag cross correlations (at zero time lag) were computed among buoys along the equator and on each of the best-sampled meridians (165°E, 140°W, and 110°W) for each of the three sets of time series. Unlike the timescale computations of section 5, where a full set of ACF lags were available for integration, cross correlations could be found only for a limited set of spatial lags, because of the 2°–3° latitude by 10°–15° longitude resolution of the array. As a consequence, curve fitting was required to derive the space scales. All possible pairs of locations with simultaneous observations were used, which means that the cross-correlations represent different time periods and record

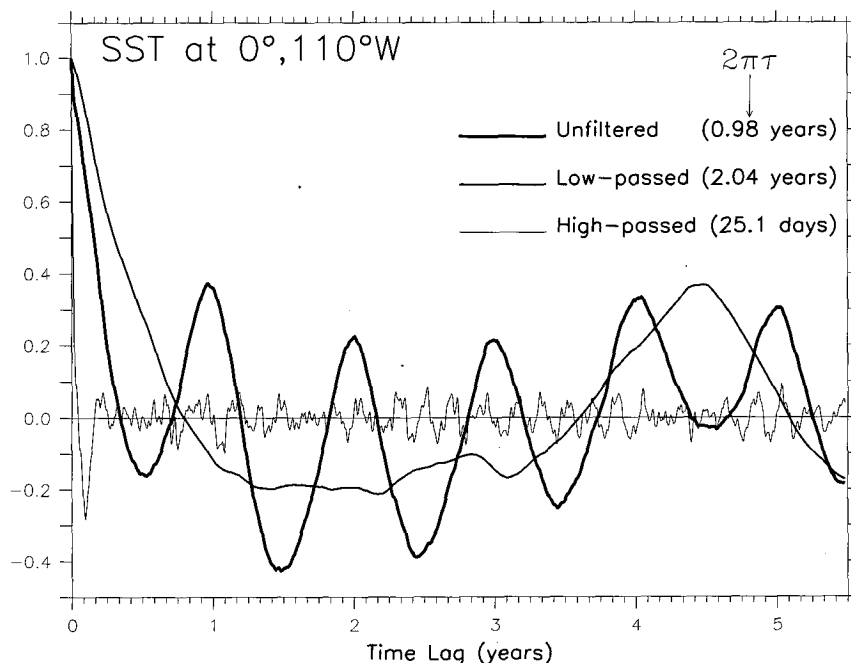


FIG. 9. Autocorrelation functions (ACFs) of SST at 0°, 110°W for three data versions: the detrended, unfiltered daily time series (heavy line), the de-seasoned (first three annual harmonics removed) then low-passed (half-power at 150-day period) time series (medium line), and the high-passed time series (thin line). The timescale shown in the legend is $2\pi\tau$, where τ is defined as the integral to the first zero-crossing of the ACF.

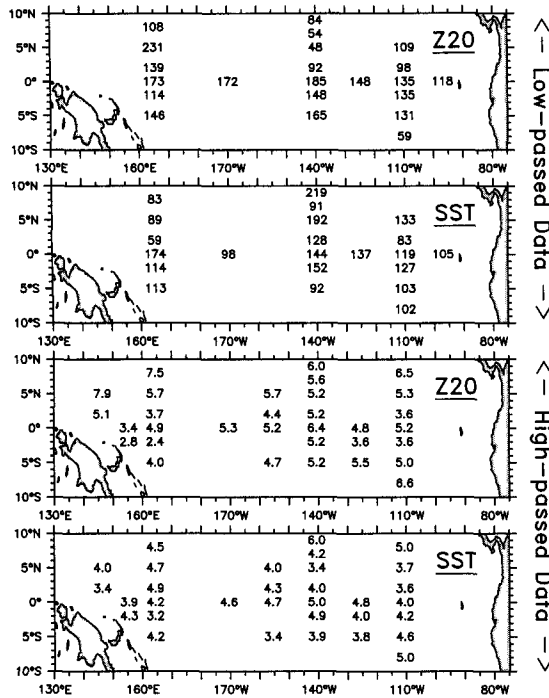


FIG. 10. Timescales (days) of low-passed (top two panels) and high-passed (bottom two panels) SST and Z20 at each buoy location (see text).

lengths. To account for this inhomogeneity, in the curve fitting each correlation was weighted according to its significance level as follows: A correlation coefficient r , with n_f degrees of freedom, may be transformed to a variable z , approximately normally distributed with standard deviation σ_z (Panofsky and Brier 1968):

$$z = \frac{1}{2} \ln \left(\frac{1+r}{1-r} \right); \quad \sigma_z = \frac{1}{\sqrt{n_f - 3}}. \quad (4)$$

This transformation, together with its inverse $r = \tanh(z)$, are commonly used in constructing confidence intervals for the correlation coefficient and suggest that in the weighted nonlinear curve fit of \tilde{r} to the observed cross-correlations r_i ,

$$\chi^2 = \sum_i w_i (r_i - \tilde{r}_i)^2, \quad (5)$$

a suitable weight would be $w_i = \sigma_z^{-2} = n_f - 3$. The number of degrees of freedom associated with each correlation value was obtained by dividing the number of cross-product terms (common days for the daily time series) by the independence timescale (Davis 1976):

$$\tau_{ij} = \Delta t \sum_k C_{ii}(k\Delta t) C_{jj}(k\Delta t), \quad (6)$$

where the subscripts i and j refer to the locations of the station pair, and $C_{ii}(k\Delta t)$ is the autocorrelation at sta-

tion i for lag $k\Delta t$. In practice, the product of autocorrelations in (6) was summed to no more than 2000-days lag. Equations (4) then give the 90% confidence range $z \pm 1.645\sigma_z$, which is transformed to the error bar associated with each correlation in Figs. 11 and 12; station pairs with a long common period generally have a narrower confidence range. The analytic functions were not forced to pass through the value unity at zero lag.

To find a space scale, the correlations were considered as a function only of station separation, and a functional form is sought that can be used to describe the falloff of correlation with distance. A large variety of functions have been used for this purpose (Alaka and Elvander 1972; MPSS; Denman and Freeland 1985), and we tried a number of experiments to find analytic functions that efficiently described the observed correlation structure. We found that many of the correlation patterns could be fit well using a simple exponential $A \exp\{-x/L\}$, giving scale estimates L (where x is the station separation and A is the value at the origin). However, the zonal Z20 correlation values, in particular, often crossed zero in a well-defined manner that was not well represented by the exponential form (e.g., the Z20 correlations in Fig. 11). This was probably due to the dominance of equatorial Kelvin and Rossby waves in the thermocline depth variability, which produced significant negative correlations between buoys more than a quarter-wavelength apart. Therefore, when such organized negative correlations were found, the functional form $A \cos(x/L_1) \exp\{-x/L_2\}$ was used. The length scale L in these cases was estimated as the integral to the first zero crossing of the cosine-exponential function, which can be expressed analytically as

$$L = L_1 L_2 \left[L_2 \exp\left(-\frac{\pi L_1}{2 L_2}\right) + L_1 \right] / (L_1^2 + L_2^2). \quad (7)$$

These scales were not much different from those found by using the simpler exponential or Gaussian forms, although the fit itself was much better.

b. Zonal scales

Figure 11 shows the cross-correlations, functional fitting, and estimated zonal scales of SST and Z20 along the equator in the three frequency ranges. The most prominent result is that the zonal scale of low-passed equatorial SST was much larger (by a factor of ~ 4) than that of Z20, which we attribute to the wave-like nature of the Z20 variability. The SST variability for the unfiltered data, which was largely due to the annual cycle (e.g., Fig. 9), was found to have a scale of about 72° longitude, consistent with the size of the equatorial cold tongue region where there is a large annual cycle of SST. The low-passed SST (essentially the ENSO signal) (Fig. 9) was fully basin scale (L

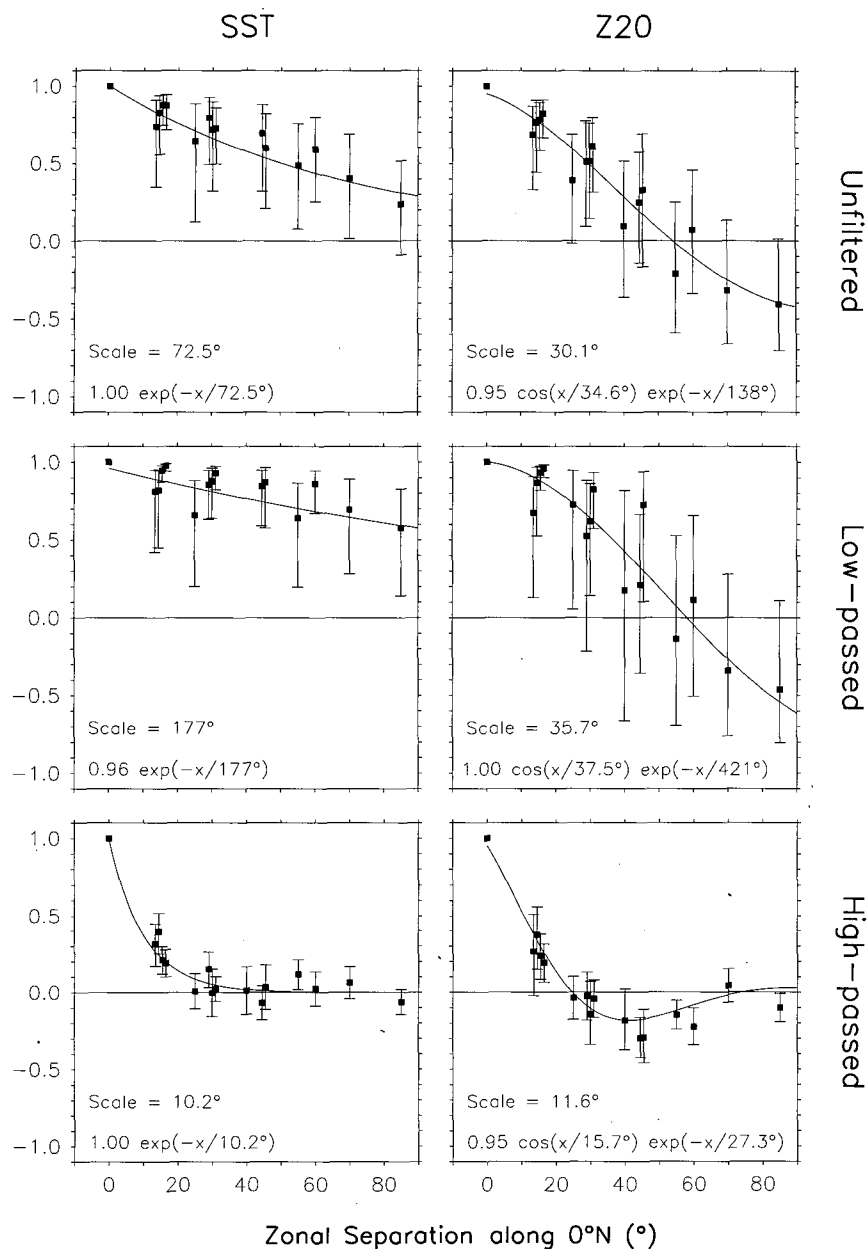


FIG. 11. Spatial lag correlations of SST (left) and Z20 (right) along the equator, plotted as a function of zonal separation, in the same three frequency partitions as in Fig. 9. Each small square shows a correlation value between a buoy pair, and the "error bars" indicate the 90% confidence range for each correlation, according to Eq. (4). The smooth curve is an analytic function fit to the correlations; the form and parameter values of these functions are given at the bottom of each panel (see text). The zonal-scale estimate is the scale of the exponent for SST, and the integral to the first zero-crossing for Z20, as indicated in each panel.

> 100° longitude), with correlations decreasing only to about 0.5 over the entire zonal extent of the TAO array (Fig. 11). The unfiltered and low-passed Z20 correlation patterns were negative at a spacing greater than 50° longitude (Fig. 11), and were fit with the combined cosine-exponential function. Both signals were found

to have a zonal scale of 30°–35°. However, the value of the fitted parameter L_1 , which scales the cosine in the functional fit, gives an implied wavelength of $2\pi L_1$. This wavelength was about 200° for both low-frequency Z20 bands, showing that, although the scales were relatively short (which suggests the station spac-

ing needed to monitor the signal), the variability itself was basin scale.

At higher frequencies, the SST and Z20 equatorial zonal scales were similar (Fig. 11), but probably for different reasons. The high-passed Z20 scale of 11.6° apparently represents the intraseasonal Kelvin waves. This zonal scale divided by the 5-day high-passed time scale (Fig. 10) implies a Kelvin-like speed of $\Delta x / \Delta t = 3 \text{ m s}^{-1}$. For the high-passed Z20 data, the combined trigonometric-exponential function was best fit with a wavelength of $2\pi L_1 = 98^\circ$, which would be consistent with a roughly 50-day period Kelvin wave, as are commonly observed (Kessler et al. 1995). The high-passed SST variability is probably strongly influenced by tropical instability waves (note that these calculations have been performed with daily average data that eliminates the large-amplitude diurnal cycle seen in Figs. 4a and 4b); however, the TIW zonal variations are only poorly resolved by the TAO array, since these waves have a zonal wavelength of only 1000–1500 km (Pullen et al. 1987). One wavelength fits within the 15° longitude zonal separation of the buoys, and therefore the zonal cross-correlations can be badly aliased. This suggests that the zonal SST correlation structure shown in Fig. 11 (lower left) probably is not truly representative of the actual variation of correlation with zonal separation. It is likely that there is a region of small or negative correlation closer than 15° separation, which cannot be resolved using the buoys. Therefore, the true zonal scale may be shorter than indicated by the buoy correlations.

c. Meridional scales

Meridional length scales were estimated in the same way as the zonal scales, fitting exponential functions to the cross-correlations between buoys along the meridians 110°W and 165°E where simultaneous time series (longer than $2\frac{1}{2}$ years) exist. The maximum distance over which cross-correlations could be found was 13° (Fig. 1). However, in several instances where correlations remained high over the entire latitude span of the array, meridional scales larger than this were estimated. Figures 12a,b show the correlations and functional fitting at 110°W and 165°E respectively. Correlations are shown strictly as a function of meridional separation, so that no distinction is made concerning position relative to the equator.

At 110°W , the unfiltered time series of SST are primarily annual (Fig. 4a), and the correlations remain very high ($r > 0.8$) over 8°S to 5°N (Fig. 12a). This is due to the large amplitude annual waxing and waning of the east Pacific cold tongue (Horel 1982). The fit to exponential functions gives scales much wider than the width of the buoy array, so the exact values are not meaningful; nevertheless, it is clear that the meridional length scale in this frequency band is at least 15° latitude (Fig. 12a). In contrast, the meridional correlation

structure of Z20 at 110°W falls off clearly within the buoy region, giving a scale of about 5° latitude (Fig. 12a). Low-passing of SST removes the annual cycle, which has large amplitude and broad meridional correlation in the cold tongue, giving smaller meridional scales at 110°W . By contrast, low passing of Z20 removes the tightly equatorially trapped Kelvin waves, increasing the meridional scales in this frequency range. For high-passed time series at 110°W , the scales for both SST and Z20 are about 2° latitude (Fig. 12a). These high-passed scales indicate that the buoy separation in the TAO array is not quite sufficient to resolve the meridional structure in this band and are consistent with studies using VOS XBT data, which often have binned the observations in 1° – 2° boxes for gridding.

At 165°E in the western Pacific, the unfiltered meridional scale of SST was smaller than in the east, apparently reflecting the weaker annual cycle of western SST and the higher proportion of variance associated with features smaller than the east Pacific cold tongue. Z20 meridional low-passed scales were comparable to those in the east. The five low individual correlation values in the upper and middle right panels of Fig. 12b all involve the mooring at 8°N , 165°E , showing the loss of low-frequency thermocline depth correlation across the North Equatorial Countercurrent, as has been previously noted (Wyrski 1978; Kessler and Taft 1987). The other pairs of low-pass Z20 cross-correlations at 165°E show that the thermocline depths in the waveguide region (5°S to 5°N) are highly correlated ($r > 0.7$) at low frequency. The high-passed scale for the west Pacific Z20 (about 2°) is similar to that in the east, but the high-passed SST scale was at least twice as large. This is probably related to the absence in the western Pacific of SST variations associated with tropical instability waves.

The ratio of zonal to meridional scales is of interest in connection with the choice of bin size for gridding irregularly spaced data products, such as VOS XBT data or observations from drifting buoys. Investigators studying low-frequency variations have commonly assumed that the zonal scales are larger than the meridional scales, often by a factor of ~ 5 , and binned point observations accordingly (e.g., Meyers 1979; Delcroix and Henin 1989; Kessler and McCreary 1993; Donoso et al. 1994; Bi 1995). Considerations such as these also influenced the design of the TAO array itself (Hayes et al. 1991a). Our results in Figs. 11 and 12 suggest that these assumptions are reasonable.

7. Discussion and summary

The highly temporally resolved time series from the TAO moored buoy array are used to compute spectra of upper tropical Pacific Ocean temperature over a period range extending from minutes to several years. These spectra provide the basis for quantifying time scales of variability of surface temper-

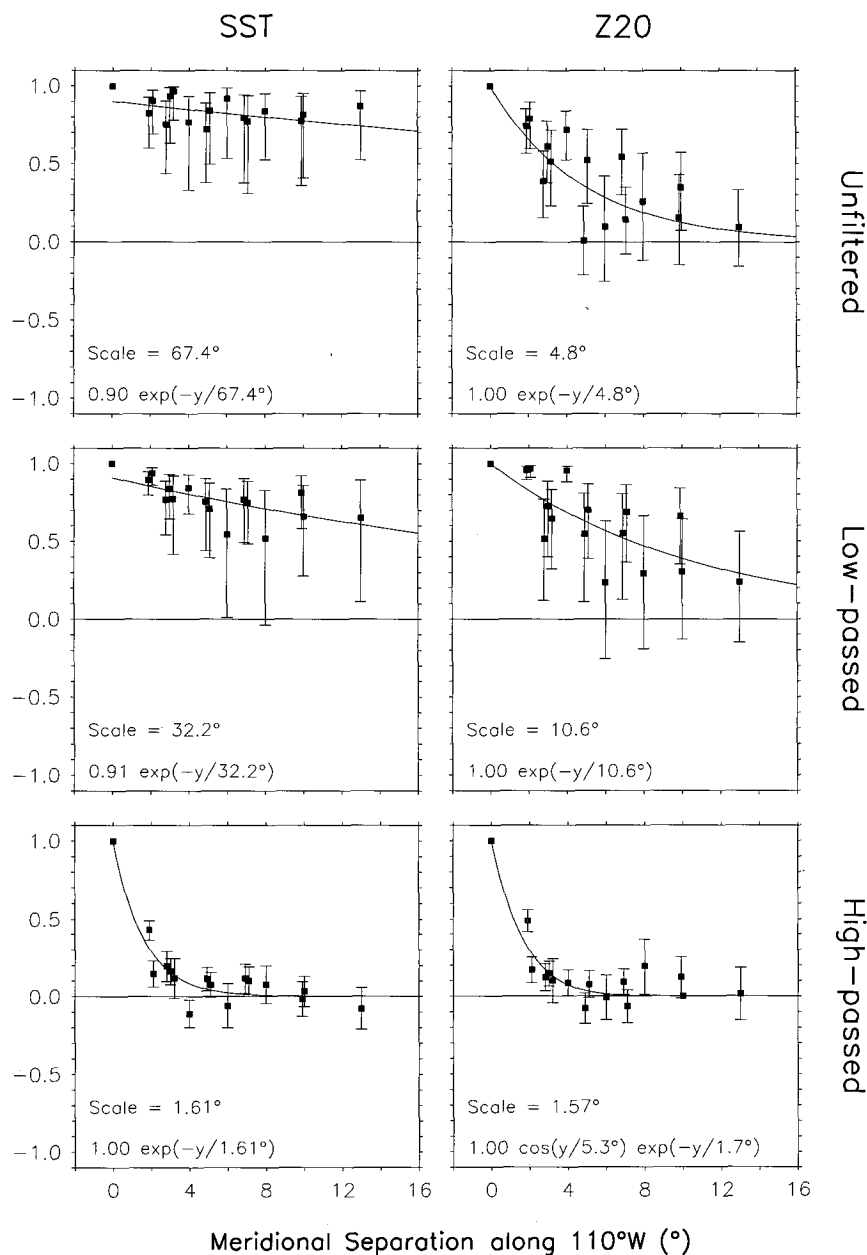


FIG. 12. (a) As in Fig. 11 but for meridional scales along 110°W.

ature and thermocline depth, and for evaluating the aliasing noise that would result from various less frequent sampling schemes. The ability to preprocess the data into unaliased seasonal cycles and low- and high-passed versions of the time series also permits stratification of temporal and spatial scale estimates by frequency band. The results allow for quantitative assessment of the ability of the Tropical Pacific Thermal Monitoring System to observe the full range of upper-ocean temperature variability.

The TAO buoy array consists of nearly 70 deep-ocean moorings arranged nominally 15° longitude and 2°–3° latitude apart across the equatorial Pacific. For most of the moorings, water temperatures are sampled every 10 minutes, then formed into daily averages that are telemetered in real time and distributed worldwide. At four current meter sites along the equator, and one off-equatorial site, a substantial amount of finer temporal sampling is available, including several months of 1-min sampling and several years of 15-min or 2-h sampling. These high-resolution records form the basis

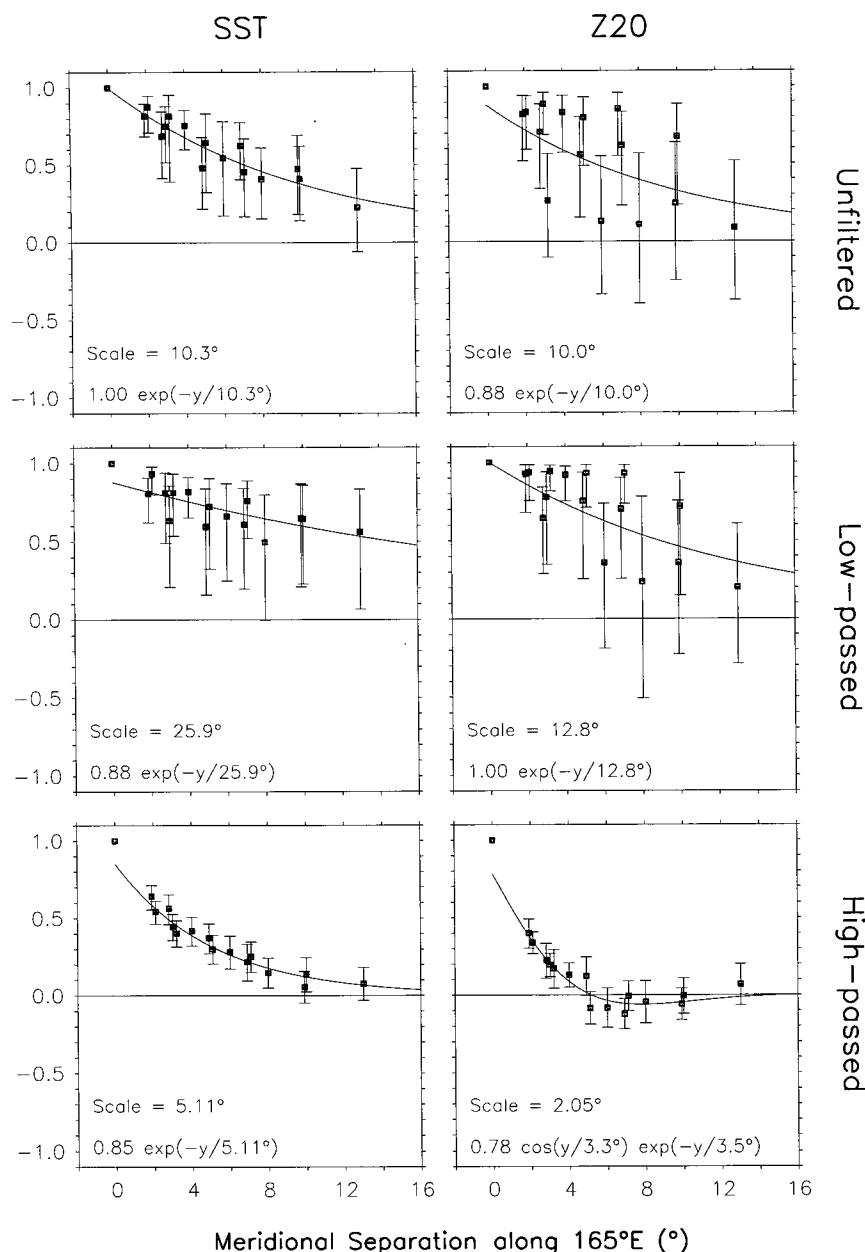


FIG. 12. (Continued) (b) As in Fig. 12a but for 165°E.

for composite spectra that span all scales of temporal variability between the Brunt-Väisälä frequency and the ENSO timescale.

The rms signal to noise ratio is a useful summary quantity that has been used by several investigators to characterize the results of sampling strategies, particularly in connection with optimal interpolation, for which the signal to noise ratio is a necessary input parameter. Earlier studies, which relied on historical datasets for the estimation of s/n, were forced by the sparseness of the existing observations

to rely on extrapolation techniques to estimate this parameter. We take advantage of the buoy time series' wide spectral range to specifically define how high-frequency variability would produce aliasing noise in hypothetical sampling regimes. This measure of aliasing can then be examined as a function both of the sampling rate and of the low frequency that is to be studied. In general, the s/n is above unity for signals with periods of a few months or longer, sampled at the nominal 20–30-day VOS XBT rate.

The signal to noise ratio is found to be larger in the eastern equatorial Pacific than in the west for both SST and thermocline depth, mostly because the low-frequency signals are larger in the east. To sample interannual variations with a s/n of 2 or greater, 100-day sampling suffices for SST both in the east and the west, but 40-day intervals are needed to achieve this signal to noise level for thermocline depth in the west. Intra-seasonal (roughly 50-day period) SST and thermocline depth variations require sampling at less than 10-day intervals for a s/n of 2. Figures 6 and 7 give the s/n for SST and Z20 as a function of sample rate and signal frequency of interest. In general, as the sample rate decreases from daily to 100-day intervals, aliasing noise increases by roughly an order of magnitude. The noise level for SST varies by as much as a factor of 10 among the locations studied, while thermocline depth noise was found to be relatively constant over the region.

We also used the buoy spectra to compute overall signal/noise ratios that represent the total daily to interannual period signal and the total noise extending to periods of hours or minutes. This quantity is simply the partition of total variance into integrated signal and noise, divided at the sampling Nyquist frequency. It is found as a function of the sample rate alone and would be the value used to characterize a sampling regime for optimal interpolation. The overall signal/noise ratio is most comparable to values reported in MPSS and other studies. For 20–30-day sampling typical of the historical XBT datasets in the tropical Pacific, values were found to be about 2–3 for SST and about 2 for Z20, several times higher than those reported by MPSS (Table 3). There are two principal reasons for the discrepancy: First is that MPSS studied the period 1979–83, which encompassed the huge El Niño event of 1982–83. They excluded this time period from their scale and signal/noise estimates, arguing that a sampling strategy must be designed that is adequate to detect the smaller signals of non-El Niño periods, in particular the possibility of observing precursors of El Niño. In the present study, we are unable to select an analogous non-ENSO time period since our time series span the warm events of 1986–87, 1991–92, and 1993, as well as the extreme cold event of 1988–89. However, we recomputed the overall signal/noise ratios excluding variance at periods greater than 400 days, which removed most ENSO-related variability while retaining most of the annual and higher-frequency signals. The resulting values, while somewhat lower than those found using all variance (Table 3), were still typically twice those reported by MPSS. A second reason for the discrepancy is the different methods used to estimate signal and noise. MPSS used a procedure in which the autocorrelation functions were extrapolated from 1-month lag (their bin size) to zero lag, then the value of the extrapolated ACF was taken to be the proportion of signal variance and one minus this value to be the proportion

of unresolved noise variance (the ACF would approach one at zero lag in the absence of noise). However, test calculations using fully resolved ACFs from the buoy time series suggested that there can be a good deal of structure to the ACFs near zero lag, and such extrapolation can produce widely differing results, depending quite sensitively on how the binning is performed and the form of the extrapolating function. The spectral techniques employed here resolve the relevant variability and, thus, should produce a more reliable result. We therefore conclude that the extrapolation method used by MPSS overestimated the unresolved noise. This conclusion is in accord with intuition, which suggests that a signal to noise ratio of ~ 2 is required to get dependable findings. Numerous studies over the years using the VOS XBT datasets have shown patterns of variability highly consistent with those derived from other data sources. If the signal/noise ratio were truly less than unity, as the MPSS results suggest, then one would not expect such regularly good results. We believe that overall signal/noise ratio for tropical Pacific temperatures sampled at roughly monthly periods is in fact close to 2, and that this explains the satisfactory outcomes from descriptive and diagnostic studies using XBTs.

Timescales were estimated as the integral to the first zero crossing of the autocorrelation functions of low- and high-passed versions of the time series (the half-power of these filters was at about 150-day periods). The most striking result was that the timescale of high-passed data was close to 5 days for both SST and thermocline depth across the entire buoy region. It is not clear why these timescales should be so homogeneous, since a diverse group of processes are responsible for variability in this frequency range. However, it is worth noting that Smith and Meyers (1996) found a similar result based on an entirely different methodology. They studied the TAO and VOS XBT time series, using a statistical interpolation procedure that gave an estimate of the number of “effective observations” in these datasets. For the TAO dataset, Smith and Meyers estimated roughly two independent observations in each 10-day analysis period from the TAO set, in agreement with the result reported here.

Horizontal spatial scales were estimated from cross correlations among the longer moored time series. Although the relatively coarse spatial distribution of the buoys renders the array less suited for space-scale determination than for timescales, the ability to stratify the time series by frequency band allows further insight than would be possible from other datasets. Zonal scales of low-frequency SST along the equator were found to be basin width, while those of thermocline depth were about 30°–40° longitude. At higher frequencies (periods shorter than 150 days), the zonal scale for sampling thermocline depth variations was about 12° longitude and apparently was associated with the intraseasonal Kelvin waves with a wavelength of

$\sim 100^\circ$ longitude. The zonal scale for high-passed SST could not be well determined by the buoy array, since this quantity is strongly affected by the tropical instability waves, which are known to have a zonal wavelength of 10° – 15° longitude that cannot be resolved within the array spacing; however, the zonal scale of high-passed SST is not more than 10° longitude. Meridional scales of low-frequency SST were larger in the east where this variability was associated with waxing and waning of the equatorial cold tongue, which is well-correlated over at least 15° of latitude. In contrast, meridional scales of high-frequency SST were larger in the west, where the variability due to tropical instability waves is usually absent. Low-frequency thermocline depth variations were well correlated over the equatorial waveguide region, but decayed rapidly across the North Equatorial Countercurrent. These scale estimates tend to confirm the common assumption that zonal scales are larger than meridional scales.

In general, the space-scale estimates reported here are considerably larger than those suggested by MPSS and Sprintall and Meyers (1991), based on VOS XBT datasets. These earlier studies recommended scales of 15° longitude and 3° latitude, which represented conservative levels designed to sample the smallest scales found. However, in most locations the scale estimates based on our unfiltered time series are larger than these values by a factor of 2 or more, particularly for SST. As in the case of the signal/noise ratios discussed earlier, one difference that accounts for much of the discrepancy is that MPSS and Sprintall and Meyers (1991) excluded the 1982–83 El Niño from their quoted scale estimates, noting that these values approximately double if the large ENSO anomalies are used in the statistics. Therefore, as was done to make comparable estimates of signal/noise ratios, we high-pass filtered the buoy time series with half-power at 400-day periods to exclude the ENSO signal, then recomputed the scale estimates shown in Figs. 11 and 12. Compared to the unfiltered results (top panels of Figs. 11 and 12), these non-ENSO scales were smaller by a factor of 2 or more, and thereby in fair agreement with those of Meyers and colleagues. Zonal scales along the equator fell from 72.5° for SST and 31.1° for Z20 to 24° and 17° , respectively. Meridional scales were similarly reduced to values about 2° to 6° latitude except for SST at 110°W , which was reduced by half but still remained larger than the meridional width of the array (we note, however, that MPSS reported meridional scales of SST in the eastern equatorial Pacific only as “greater than 6° ”). Therefore, the 3° latitude by 15° longitude scale recommendation from the VOS XBT datasets is roughly consistent with the present results from the TAO buoys for non-ENSO variations. Nevertheless, it should be kept in mind that these estimates represent the scales of the dominant variability in the time series, which is usually the large-scale, low-frequency signals, even with the ENSO variations re-

moved. Our results for the 150-day high-passed time series (lower panels of Figs. 11 and 12) show that if signals with periods of 1 to 2 months are to be properly sampled, then the scales are shorter, about 1° – 2° latitude by 8° – 10° longitude, with a 5-day timescale.

Another issue that can be resolved by the buoy time series concerns the possibility that space-scale estimates from the VOS XBT data might be affected by the relatively sparse temporal sampling. We checked this by subsampling the TAO buoy time series at intervals of up to 60 days, then recomputing the spatial scales by fitting functions as in Figs. 11 and 12, repeating this calculation for many realizations of subsampling. For even 60-day subsampling, although the individual cross-correlation values comparable to the top panels of Figs. 11 and 12 were somewhat scattered, the scale estimates were relatively unchanged because the scatter of values around the functional fit were random in character. The standard deviation of scale estimates among the 60-day subsamples was generally about one-tenth the scale value itself, and never more than one-fifth the scale value. For the typical VOS XBT sample interval of 20–30 days, the standard deviations were smaller by an additional factor of 2. This suggests that scale estimates calculated from the VOS datasets are likely to be accurate. Again, this conclusion applies only to the unfiltered time series representing principally the large-scale, low-frequency phenomena; for the 150-day high-passed dataset, different realizations of 30-day subsampling produce scale estimates that differ by up to a factor of 2.

MPSS recommended a temporal decorrelation scale of 1.5 to 3 months, which is somewhat shorter than we report for the low-pass filtered buoy time series (Fig. 10, top). The MPSS values are reasonably consistent with timescales derived here from unfiltered buoy time series (not shown). We have argued above, however, that since MPSS excluded periods of strong ENSO variations, their XBT scale estimates should be comparable to buoy time series high-pass filtered with 400-day half-power. When such filtered buoy time series are used to compute timescales, the values are 10–20 days, for both SST and thermocline depth, over the entire buoy region. This suggests that variability with periods of up to a few months is unresolved noise in the XBT time series, which makes estimation of a timescale from that dataset problematic.

While we have presented many results in this first statistical summary of the temperature observations obtained with the TAO array, it is important to remember that the array has been deployed at full strength for just over one year (since December 1994). Many of the mooring sites have accumulated fewer than two years of data, and so are at best marginally useful in expanding the range of space scales over which we can evaluate reliable statistics. Our very long time series exhibit strong interannual variability, reminding us that very long records are needed to obtain robust statistics in

this part of the ocean. As the full deployment of the array continues, we plan to revisit these calculations, both to update the statistics using the longer records and to include spatial correlation results that cannot be meaningfully evaluated at this time (e.g., zonal correlations along off-equatorial latitudes).

We have emphasized the dependence of the statistical parameters on the frequency of the signal that is to be studied or monitored. Sampling requirements are several times more stringent if fluctuations with periods of 1–2 months must be resolved than if only 150-day or longer period signals are significant. Our calculations of the noise variance due to sampling at different rates in different locations provide a basis for tailoring an observational strategy to the s/n level needed in the measurement of a particular quantity. Thus, our results are relevant not only for evaluations of the existing observing system in the tropical Pacific, but also in a general sense for the design of future observing systems in other parts of the World Ocean.

Acknowledgments. The authors dedicate this paper to their late friend and colleague, Stan Hayes. The existence of the TAO array on which this study depends is due largely to Stan's vision and perseverance. Stan inspired and helped initiate the present work, and he would have been coauthor of this paper were it not for his untimely passing.

We would like to thank the TAO group at NOAA/PMEL for processing the raw data and preparing formatted datasets. We have benefited greatly from discussions with Gary Meyers, Shoichiro Nakamoto, Dean Roemmich, and Neville Smith. Funding for this work was provided by NOAA's Office of Global Programs.

APPENDIX

Aliasing in Inverse Power Law Spectra

When a process having an inverse power law spectrum

$$S(f) = (f/f_0)^{-a}, \quad a > 1 \quad (\text{A1})$$

over all frequencies is sampled at regular intervals Δt , the noise aliased from beyond the Nyquist frequency $f_0 = 1/2\Delta t$ is, by Eq. (1),

$$N(f) = \sum_{k=1}^{\infty} [(2k - f/f_0)^{-a} + (2k + f/f_0)^{-a}]. \quad (\text{A2})$$

The noise increases monotonically with frequency from

$$N_0 = \lim_{f \rightarrow 0} N(f) = 2^{1-a} \sum_{k=1}^{\infty} k^{-a} \quad (\text{A3})$$

to

$$N_1 = \lim_{f \rightarrow f_0} N(f) = 2 \sum_{k=0}^{\infty} (2k+1)^{-a}. \quad (\text{A4})$$

The sums of reciprocal powers in Eqs. (A3) and (A4) can be expressed in terms of the Riemann zeta function $\zeta(a)$ (Bender and Orszag 1978, chapter 8.1). While, as might be expected, the noise level increases as the underlying spectrum becomes less steep ($a \rightarrow 1$), the noise range $N_1 - N_0$ decreases. In other words the noise spectrum associated with aliasing becomes whiter when the exponent of the power law is reduced.

This is illustrated for a range of exponents between $a = 1.5$ and $a = 2.5$ in Fig. A1. Straight (solid) lines in log-log space represent the underlying power law spectra $S(f)$. These are truncated for clarity, though in reality they extend offscale. The dash-dot curves show the noise spectra due to aliasing when a process with $S(f) = (f/f_0)^{-2.5}$ is sampled at regular intervals $\Delta t = 1, 2, 4, 8, 16, 32, 64$. The range (which is common to all the noise curves for $a = 2.5$) is shown as a bar in the lower right corner. The narrow range of the noise spectrum (for regular sampling) over several decades

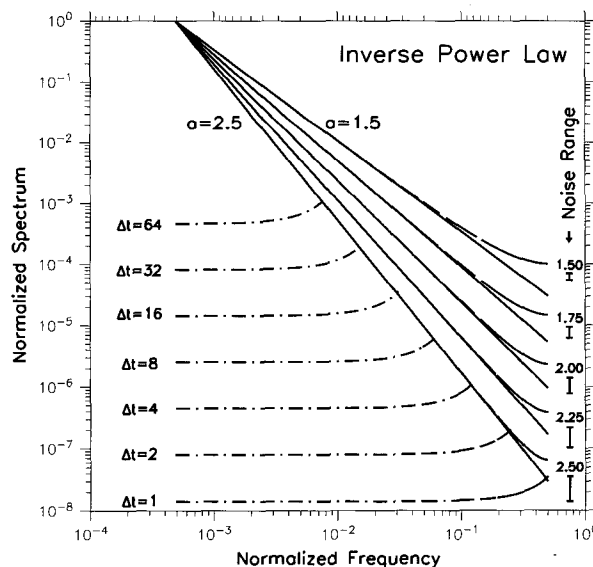


FIG. A1. Illustration of noise due to sparse sampling of idealized inverse power law spectra. Straight solid lines are fully resolved idealized spectra, representing exponents between $a = 1.5$ and $a = 2.5$ in steps of 0.25. The dash-dot curves show the noise spectra, computed from Eq. (A2), resulting from aliasing when a process with spectrum $f^{-2.5}$ is sampled at regular intervals $\Delta t = 1, 2, 4, 8, 16, 32$, and 64 time units. The range of values this noise takes over all low frequencies is shown as the bar in the lower right corner; this range is the same for all the sampling rates for the $a = 2.5$ spectrum. The other bars along the right edge show the noise ranges for each of the other idealized spectra. The dashed lines that diverge from each base spectrum show the aliased spectra that would be measured given sampling at $\Delta t = 1$. At each frequency, the aliased spectral values are the sum of the true spectrum and the aliasing.

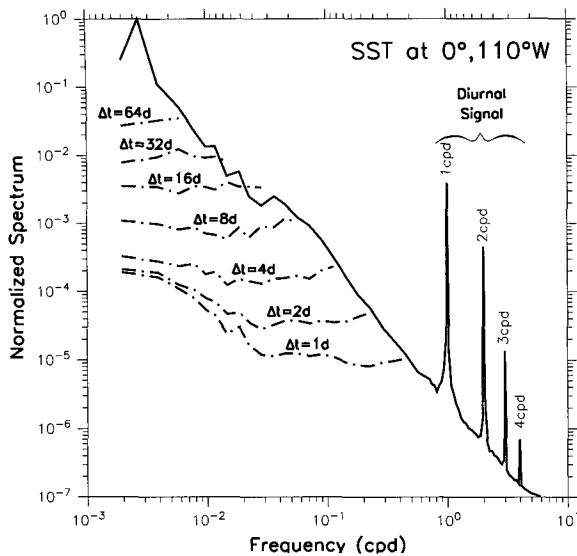


FIG. A2. Similar to Fig. A1 but based on the observed SST at 0°, 110°W (2-h samples), subsampled at various rates Δt . Harmonics of the diurnal cycle are labeled peaks. As in Fig. A1, the dash-dot lines show the noise spectra at low frequencies resulting from each sampling rate.

of frequency explains why the signal-to-noise contours of Fig. 6 are parallel and are essentially scaled replicates of the signal spectrum itself. The aliased spectrum (given sampling at $\Delta t = 1$) is shown as the dashed line branching off from the true $a = 2.5$ spectrum. This curve is the sum of the true and noise spectrum at each frequency. The aliasing noise is seen to be white everywhere except quite near the Nyquist frequency (where $f_p \approx f_0$).

For the other underlying spectra in Fig. A1, the noise spectra are similar in form, but with higher level and narrower range, to those illustrated for $a = 2.5$. Bars along the right edge show the noise ranges for the other underlying spectra shown, with exponents a decreasing in steps of 0.25 to the value $a = 1.5$. A spectrum with exponent $a \approx 1.5$ is representative of much of the frequency dependence of SST and Z20 in the tropical Pacific (see section 4). The range of each noise spectrum decreases with decreasing a , as indicated by the bars, however, the noise level becomes larger. The aliased spectra in each case for sampling at $\Delta t = 1$ (dashed curves branching from the true spectra) show the relatively larger error that extends over an increasing range of frequencies with decreasing exponent a .

The noise spectra associated with aliasing of observed SST at 0°, 110°W are shown in Fig. A2 for sampling intervals of 1, 2, 4, 8, 16, 32, and 64 days. The underlying spectrum, computed from 8 years of 2-h data (solid curve) varies approximately as f^{-2} for periods shorter than about 15 days. For periods between 15 days and the annual period the spectrum is close to $f^{-1.6}$. The noise spectra (dash-dot lines) for sampling

at $\Delta t \geq 4$ days are nearly white, as predicted by the theoretical argument above. However, noise in the 1- and 2-day sampled time series is larger than expected at low frequencies, due to the presence of strong diurnal variability. As is evident in Fig. 4, SST has a strong diurnal cycle with a nonsinusoidal waveform and an amplitude that is nonstationary in time. This results in a family of harmonics in the spectrum, with noticeable cusps. For sampling at integral multiples of 1 day, as in our examples, the energy at 1, 2, 3, . . . cycles per day aliases into the mean and does not appear in the noise spectra (dot-dash curves). The energy from the cusps, however, folds primarily into the lower Fourier frequencies and distorts the noise spectrum from the white form that would otherwise be expected. This is particularly noticeable for $\Delta t = 1$ and 2 days; with sparser sampling these diurnal peaks are a less dominant source of noise; energy aliased from other parts of the unresolved spectrum makes the noise spectra whiter.

REFERENCES

- Alaka, M. A., and R. C. Elvander, 1972: Optimum interpolation from observations of mixed quality. *Mon. Wea. Rev.*, **100**, 612–624.
- Barnett, T. P., and W. C. Patzert, 1980: Scales of thermal variability in the tropical Pacific. *J. Phys. Oceanogr.*, **10**, 529–540.
- Bender, C. M., and S. Orszag, 1978: *Advanced Mathematical Methods for Scientists and Engineers*. McGraw-Hill, 593 pp.
- Bi, K., 1995: Variability of the surface layer circulation in the western equatorial Pacific. Ph.D. dissertation, Scripps Institution of Oceanography, 175 pp.
- Bretherton, F. P., R. E. Davis, and C. B. Fandry, 1976: A technique for objective analysis and design of oceanographic experiments applied to MODE-73. *Deep-Sea Res.*, **23**, 559–582.
- Chang, P., 1993: Seasonal cycle of sea surface temperature and mixed layer heat budget in the tropical Pacific Ocean. *Geophys. Res. Lett.*, **20**, 2079–2082.
- Davis, R. E., 1976: Predictability of sea surface temperature and sea level pressure anomalies over the North Pacific Ocean. *J. Phys. Oceanogr.*, **6**, 249–266.
- Delcroix, T., and C. Henin, 1989: Mechanisms of subsurface thermal structure and sea surface thermohaline variability in the south-west tropical Pacific during 1975–85. *J. Mar. Res.*, **47**, 777–812.
- Denman, K. L., and H. J. Freeman, 1985: Correlation scales, objective mapping, and a statistical test of geostrophy over the continental shelf. *J. Mar. Res.*, **43**, 517–539.
- Donoso, M. C., J. E. Harris, and D. B. Enfield, 1994: Upper ocean thermal structure of the eastern tropical Pacific. NOAA Tech. Rep. ERL-450-AOML. U.S. Dept. of Commerce, 226 pp.
- Eriksen, C. C., 1982: Equatorial wave vertical modes observed in a western Pacific island array. *J. Phys. Oceanogr.*, **12**, 1206–1227.
- Freitag, H. P., M. J. McPhaden, and A. J. Shepherd, 1987: Equatorial current and temperature data: 108°W to 110°W: October 1979 to November 1983. NOAA Tech. Memo. ERL-PMEL-17, 99 pp.
- Gandin, L. S., 1963: *Objective Analysis of Meteorological Fields*. Hydrometeorological Publishing, Leningrad, 1963. (English translation by: Israeli Program for Scientific Translations, Jerusalem, 1965; available from US Dept. of Commerce, Clearinghouse for Federal Scientific and Technical Information, Springfield, VA 22151).
- Halpern, D., R. A. Knox, and D. S. Luther, 1988: Observations of 20-day period meridional current oscillations in the upper ocean along the Pacific equator. *J. Phys. Oceanogr.*, **18**, 1514–1534.

- Hansen, D. V., and C. A. Paul, 1984: Genesis and effect of long waves in the equatorial Pacific. *J. Geophys. Res.*, **89**, 10 431–10 440.
- Hayes, S. P., and M. J. McPhaden, 1992: Temporal sampling requirements for low-frequency temperature variability in the eastern equatorial Pacific Ocean. NOAA Tech. Memo. ERL-PMEL-96, 17 pp.
- , —, and A. Leetmaa, 1989: Observational verification of a quasi-real-time simulation of the tropical Pacific Ocean. *J. Geophys. Res.*, **94**, 2147–2157.
- , L. J. Mangum, J. Picaut, A. Sumi, and K. Takeuchi, 1991a: TOGA-TAO: A moored array for real-time measurements in the tropical Pacific Ocean. *Bull. Amer. Meteor. Soc.*, **72**, 339–347.
- , P. Chang, and M. J. McPhaden, 1991b: Variability of the sea surface temperature in the eastern equatorial Pacific during 1986–1988. *J. Geophys. Res.*, **96**, 10 553–10 566.
- Horel, J. D., 1982: On the annual cycle of the tropical Pacific atmosphere and ocean. *Mon. Wea. Rev.*, **110**, 1863–1878.
- Ji, M., A. Leetmaa, and J. Derber, 1995: An ocean analysis system for climate studies. *Mon. Wea. Rev.*, **123**, 460–481.
- Kessler, W. S., 1990: Observations of long Rossby waves in the northern tropical Pacific. *J. Geophys. Res.*, **95**, 5183–5217.
- , and B. A. Taft, 1987: Dynamic heights and zonal geostrophic transports in the central tropical Pacific during 1979–1985. *J. Phys. Oceanogr.*, **17**, 97–122.
- , and J. P. McCreary, 1993: The annual wind-driven Rossby wave in the subthermocline equatorial Pacific. *J. Phys. Oceanogr.*, **23**, 1192–1207.
- , B. A. Taft, and M. J. McPhaden, 1985: Assessment of the XBT sampling network in the central Pacific. Univ. Corp. Atmos. Res., US TOGA 4, 62 pp.
- , M. J. McPhaden, and K. M. Weickmann, 1995: Forcing of intraseasonal Kelvin waves in the equatorial Pacific. *J. Geophys. Res.*, **100**, 10 613–10 631.
- Levine, M. D., 1981: Dynamic response of the VACM temperature sensor. *Deep-Sea Res.*, **28A**, 1401–1408.
- Mangum, L. J., H. P. Freitag, and M. J. McPhaden, 1994: TOGA-TAO array sampling schemes and sensor evaluations. *Proc. Oceans '94 OSATES*, Vol. II, Brest, France, 402–406.
- McCarty, M. E., and M. J. McPhaden, 1993: Mean seasonal cycles and interannual variations at 0°, 165°E during 1986–1992. NOAA Tech. Memo. ERL-PMEL-98, 64 pp.
- McPhaden, M. J., 1993: TOGA-TAO and the 1991–93 El Niño–Southern Oscillation event. *Oceanography*, **6**, 36–44.
- , 1995: The Tropical Atmosphere–Ocean array is completed. *Bull. Amer. Meteor. Soc.*, **76**, 739–741.
- , and S. P. Hayes, 1990: Variability in the eastern equatorial Pacific Ocean during 1986–1988. *J. Geophys. Res.*, **95**, 13 195–13 208.
- , and M. E. McCarty, 1992: Mean seasonal cycles and interannual variations at 0°, 110°W and 0°, 140°W during 1980–1991. NOAA Tech. Memo. ERL-PMEL-95, 118 pp.
- , A. J. Busalacchi, J. Picaut, and G. Raymond, 1988: A model study of potential sampling errors due to data scatter around expendable bathythermograph transects in the tropical Pacific. *J. Geophys. Res.*, **93**, 8119–8130.
- Meyers, G., 1979: On the annual Rossby wave in the tropical North Pacific Ocean. *J. Phys. Oceanogr.*, **9**, 663–674.
- , and J.-R. Donguy, 1980: An XBT network with merchant ships. *Trop. Ocean–Atmos. Newslett.*, **2**, 6–7.
- , H. Phillips, N. Smith, and J. Sprintall, 1991: Space and time scales for optimal interpolation of temperature—Tropical Pacific Ocean. *Progress in Oceanography*, Vol. 28, Pergamon, 189–218.
- Panofsky, H. A., and G. W. Brier, 1968: *Some Applications of Statistics to Meteorology*. University of Pennsylvania Press, 224 pp.
- Pullen, P. E., R. L. Bernstein, and D. Halpern, 1987: Equatorial long-wave characteristics determined from satellite sea surface temperature and in situ data. *J. Geophys. Res.*, **92**, 742–748.
- Rebert, J. P., J.-R. Donguy, G. Eldin, and K. Wyrtki, 1985: Relations between sea level, thermocline depth, heat content and dynamic height in the tropical Pacific Ocean. *J. Geophys. Res.*, **90**, 11 719–11 725.
- Reynolds, R. W., and T. M. Smith, 1994: Improved sea surface temperature analyses using optimum interpolation. *J. Climate*, **7**, 929–948.
- Roemmich, D., 1983: Optimal estimation of hydrographic station data and derived fields. *J. Phys. Oceanogr.*, **13**, 1544–1549.
- Smith, N. R., and G. Meyers, 1996: A comparison of VOS XBT and TOGA-TAO data. *J. Geophys. Res.*, in press.
- Sprintall, J., and G. Meyers, 1991: An optimal XBT sampling network for the eastern Pacific Ocean. *J. Geophys. Res.*, **96**, 10 539–10 552.
- Stammer, D., and C. W. Böning, 1992: Mesoscale variability in the Atlantic Ocean from Geosat altimetry and WOCE high-resolution numerical modeling. *J. Phys. Oceanogr.*, **22**, 732–752.
- Taft, B. A., and M. J. McPhaden, 1990: Diurnal cycle of sea surface temperature in the western tropical Pacific. *Proc. Symp. on U.S./P.R.C. Bilateral Air-Sea Interaction Program*. Beijing, China, NOAA, 343–352.
- Weisberg, R. B., and A. M. Horigan, 1981: Low-frequency variability in the equatorial Atlantic. *J. Phys. Oceanogr.*, **11**, 913–920.
- White, W. B., and R. L. Bernstein, 1979: Design of an oceanographic network in the midlatitude North Pacific. *J. Phys. Oceanogr.*, **9**, 592–606.
- , G. Meyers, and K. Hasanuma, 1982: Space/time statistics of short-term climatic variability in the western North Pacific. *J. Geophys. Res.*, **87**, 1979–1989.
- Wunsch, K., and A. E. Gill, 1976: Observations of equatorially-trapped waves in Pacific sea level variations. *Deep-Sea Res.*, **23**, 371–390.
- Wyrtki, K., 1978: Sea level variations: Monitoring the breath of the Pacific. *Eos, Trans. Amer. Geophys. Union*, **60**, 25–27.
- , E. Firing, R. Knox, G. J. McNally, W. C. Patzert, E. D. Stroup, B. A. Taft, and R. Williams, 1981: The Hawaii-to-Tahiti Shuttle Experiment. *Science*, **211**, 22–28.